



Performance evaluation of supersonic flow for variable geometry radial ejector through CFD models based on DES-turbulence models, GPR machine learning, and MPA optimization

Raed Al-Rbaihat^{a,b,*}, Khalid Saleh^a, Ray Malpress^a, David Buttsworth^a, Hussein Alahmer^c, Ali Alahmer^{b,d,*}

^a School of Mechanical and Electrical Engineering, University of Southern Queensland, Queensland 4350, Australia

^b Department of Mechanical Engineering, Faculty of Engineering, Tafila Technical University, P. O. Box 179, 66110 Tafila, Jordan

^c Department of Automated Systems, Faculty of Artificial Intelligence, Al-Balqa Applied University, Al-Salt 19117, Jordan

^d Department of Industrial and Systems Engineering, Auburn University, Auburn, AL 36849, United States

ARTICLE INFO

Keywords:

Radial flow ejectors
Supersonic flow
RANS turbulence models
Detached eddy simulation
Gaussian process regression
Machine learning
Marine Predators algorithm

ABSTRACT

This study aims to derive valuable insights for utilizing computational fluid dynamics (CFD) based on reynolds-averaged navier–stokes (RANS) and detached eddy simulation (DES) turbulence models (TMs) to analyze a specific radial ejector configuration known as the variable geometry radial ejector (VGRE). The VGRE features the primary nozzle and ejector duct plates with adjustable disk-like surfaces, allowing for changes in the nozzle and ejector throat areas within a single ejector. Extensive numerical investigations of the VGRE are conducted by systematically validating CFD models with experimental datasets and subsequently using the most appropriate TM to design a new radial ejector. The study reveals that the DES SST $k-\omega$ turbulence model achieves the closest agreement with experimental data, with an average entrainment ratio (ω) discrepancy of only 5%. However, there are challenges in accurately predicting the critical compression ratio (r_c^*), especially under varying conditions. Based on the CFD results, the original VGRE exhibited ω values ranging from 0.16 to 0.61, r_c^* values between 1.5 and 3.1, and ejector efficiency (η) values between 7% and 17% at expansion ratio (r_e) values ranging from 89 to 150 for different nozzle throat separations (d) and different duct throat separations (D). Furthermore, this study presents a comprehensive investigation into predicting and optimizing ω , r_c^* , and η parameters using a multi-output gaussian process regression (GPR) model and a marine predators algorithm (MPA) approach. The multi-output GPR model was constructed to predict the relationships between boundary conditions (primary pressure (P_{primary}) and secondary pressure ($P_{\text{secondary}}$)), geometric parameters (d and D), and the response variables (ω , r_c^* , and η). The model evaluation employed a 5-fold cross-validation technique to assess predictive performance, demonstrating strong predictive accuracy with low root mean square error (RMSE) and high coefficient of determination (R^2) values. The optimization results revealed that the highest achieved values were $\omega = 0.303$, $r_c^* = 2.678$, and $\eta = 0.156$, corresponding to specific parameter settings ($P_{\text{primary}} = 160$ kPa, $P_{\text{secondary}} = 1.8$ kPa, $d = 0.6$ mm, and $D = 2.3$ mm). This study demonstrates the effectiveness of the multi-output GPR model for accurate prediction and the multi-objective MPA optimization approach for identifying optimal input parameters to maximize entrainment ratio, critical compression ratio, and ejector efficiency in fluid dynamics systems.

1. Introduction

Ejectors, a technology gaining significant attention, exhibit promise in harnessing energy from low-grade sources like solar energy and waste heat for power generation [1–6]. Distinguished by their elegant

simplicity, ejectors utilize a high-energy primary flow to induce movement in a low-pressure secondary flow, essentially functioning as compressors without moving parts [7,8]. The challenge in solar-powered ejector cooling systems lies in fixed-geometry ejectors struggling under conditions deviating from design parameters. In contrast, a variable geometry ejector offers an expanded operational range, accommodating

* Corresponding authors.

E-mail addresses: rbaihat@ttu.edu.jo (R. Al-Rbaihat), aza0300@auburn.edu (A. Alahmer).

<https://doi.org/10.1016/j.ijft.2023.100487>

Nomenclature		Y	Output of the training set
<i>Symbols</i>		y'	Prediction of the testing set
A	Constant	<i>Greek symbols</i>	
d	Nozzle throat separation (mm)	η	Ejector efficiency
d	Number of dimensions, (Section 5)	ω	Entrainment ratio
D	Duct throat separation (mm)	$\mu(x)$	Mean function
EXP	Experiments	σ	Covariance function of the Gaussian Process
l_{min}	Lower bounds	μ'	Predicted mean
l_{max}	Upper bounds	σ'	Predicted covariance
\vec{l}	Top predator vector	ε_t	Gaussian noise
Ma	Mach number	y_t	Multi-output function
\dot{m}	Mass flow rate (g/s)	\otimes	Entry-wise multiplications
$\dot{m}_{primary}$	Primary mass flow rate (g/s)	<i>Abbreviations</i>	
$\dot{m}_{secondary}$	Secondary mass flow rate (g/s)	AFA	Available flow area
N	Number of search agents	BCs	Boundary conditions
P_{out}^*	Critical outlet pressure	BSL	Baseline Reynolds model
P_{out}	Outlet pressure	CF	Convergence factor
$P_{primary}$	Primary flow pressure	CFD	Computational fluid dynamics
$P_{secondary}$	Secondary flow pressure	DES	Detached eddy simulation
P_{static}	Static pressure	EM	Elite matrix
R	Vector of uniformly distributed random values	FADs	Fish aggregating devices
R_L	Vector of random values corresponding to the Lévy movement	GPR	Gaussian process regression
R_B	Vector signifying the Brownian motion	LES	Large eddy simulation
R	Random number	ML	Machine learning
r_1, r_2	Random indexes	MPA	Marine predators algorithm
R^2	Coefficient of determination	PM	Prey matrix
r_c^*	Critical compression ratio	<i>Rand</i>	uniform random vector
r_e	Expansion ratio	RANS	Reynolds-Averaged Navier–Stokes
\vec{U}	Binary vector	RMSE	root mean square error
X	Input of the training set	SST	Shear stress transport
x'	Input of the testing set	TM	Turbulence model
		VGRE	Variable geometry radial ejector

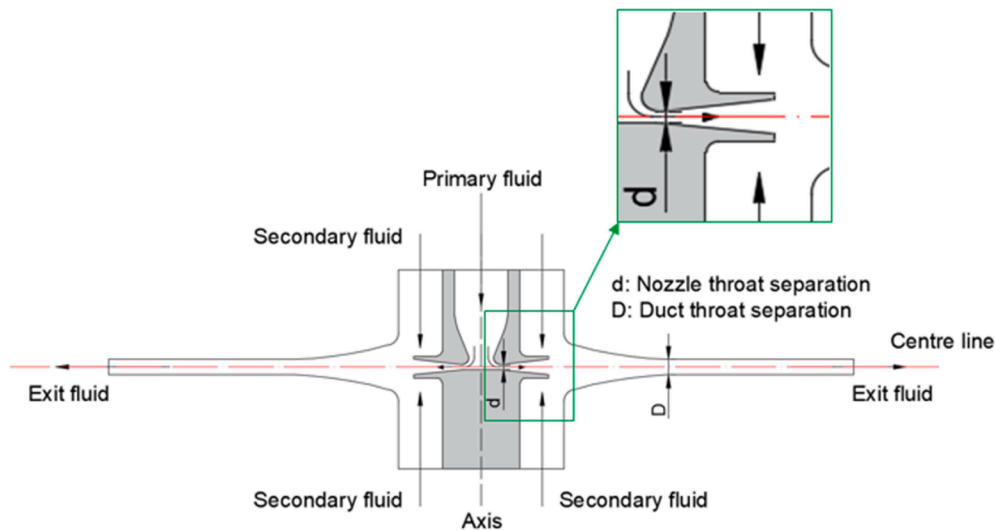


Fig. 1. Illustration of the VGRE configuration depicting the relevant flow paths [53].

variations in solar insolation and enhancing overall performance [9,10]. This adaptability is demonstrated by the ability to adjust the nozzle throat size to vary primary and secondary flows, allowing the ejector to cope with changing heat inputs [11]. The introduction of a rotary radial ejector by Garriss Jr et al. [12] aimed to improve the coefficient of

performance (COP) by eliminating shocks in the compression process, although practical confirmation faced challenges due to high rotary speeds. The variable geometry radial ejector (VGRE) configuration stands out for its praised adaptability, enabling easy adjustments without altering the ejector's surface profiles, thus presenting a versatile

Table 1
Parameters for CFD simulations of both RANS-TMs and DES-TMs.

Parameter	RANS-TMs and DES-TMs
Type of solver	Density-based
Two-Dimensional space	Axisymmetric
Temporal dimension	Transient
Equation of energy	On
Turbulence model	DES SST $k-\omega$
Material	Air (Density: Ideal gas)
Primary and secondary flow	Pressure inlet
Ejector outlet	Pressure outlet
Formulation	Implicit
Spatial discretization	Second order
Courant number	1.0
Residuals	10^{-7}
Initialization method	Hybrid
Time step size (s)	5×10^{-6}
Number of time steps	10,000
Maximum iterations per time step	150

and efficient solution.

Studies utilizing computational fluid dynamics (CFD) to explore radial ejectors have been limited. Gheorghiu and Oprisa-Stanescu [13] developed a 2-dimensional CFD model for a supersonic radial ejector, emphasizing the Realizable $k-\epsilon$ turbulence model's selection. Their findings highlighted the significance of cross-sectional area over primary nozzle shape in influencing ejector performance, ultimately concluding that radial ejectors surpass conventional axial ejectors. Ababaneh et al. [14] performed numerical assessments on an unsteady radial flow ejector equipped with a radial flow diffuser, validating their CFD results by comparing them with an analytical solution. Employing two-dimensional simulations with SST $k-\omega$ and $k-\epsilon$ standard turbulence models, they found that the $k-\epsilon$ standard model closely aligned with experimental data, especially regarding critical parameters such as entrainment ratio and critical compression ratio. Rahimi [15] proposed 2D CFD models to optimize a new Variable Geometry Radial Ejector (VGRE) configuration, using the SST $k-\omega$ turbulence model. Comparative

analysis under identical operating conditions revealed slight differences in entrainment ratios between radial and axial ejectors, with further investigations on ejector throat separation demonstrating substantial impacts on entrainment ratio and outlet pressure. Comparisons between experiments and simulations preferred the $k-\epsilon$ standard turbulence model, showing good agreement across different operating conditions with an average discrepancy of less than 16 % in entrainment ratio and critical outlet pressure.

Computational fluid dynamics (CFD) simulations have become an integral tool for designing novel ejector configurations and evaluating their performance, consistently exhibiting commendable accuracy when compared to experimental data. Extensive research has been devoted to selecting appropriate turbulence models (TMs) for CFD simulations [16–22], with a growing emphasis on the efficiency of transient simulations over steady-state ones, as they provide more robust and convergent solutions that align more effectively with experimental data [23]. Unsteady CFD simulations, notably, have shown superior accuracy in predicting the behavior of free jet flow [24]. Despite these advancements, challenges persist in establishing a consensus on the most suitable TMs for accurately simulating ejector flows [25]. Various studies indicate that disparities between experimental data and CFD simulations are significantly influenced by operating conditions [26] and working fluid [27]. Reported relative errors in axial ejectors between experimental results and computational simulations using different Reynolds-Averaged Navier–Stokes (RANS)-TMs vary significantly [28–30], ranging from approximately 25 % [31] to over 100 % in certain operating conditions [32].

Bartosiewicz et al. [33] thoroughly evaluated the performance of a supersonic ejector using a range of Reynolds-Averaged Navier–Stokes turbulence models (RANS-TMs). The SST $k-\omega$ model stood out as the preferred choice due to its superior stream mixing capabilities, particularly in predicting boundary layer separation and shock wave behavior in supersonic air ejectors. Despite a tendency to slightly overestimate shear stress between streams, the SST $k-\omega$ model consistently demonstrated prowess in various investigations [34,35]. Similarly, Besagni and

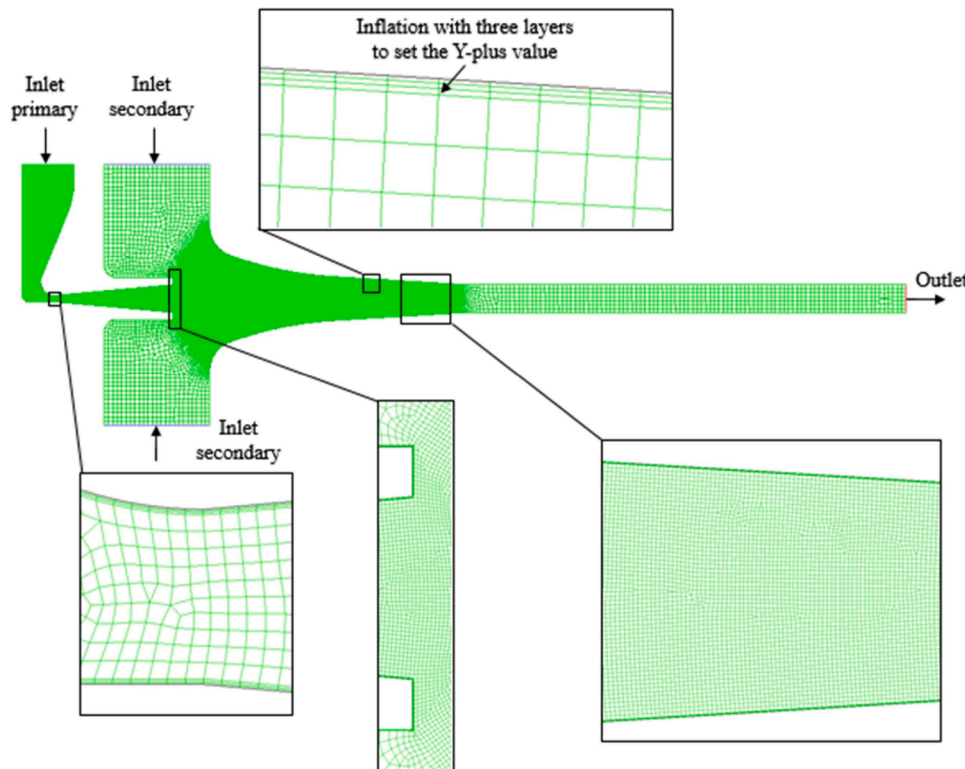


Fig. 2. Mesh grid detail for the original VGRE simulations - 70,123 Cells.

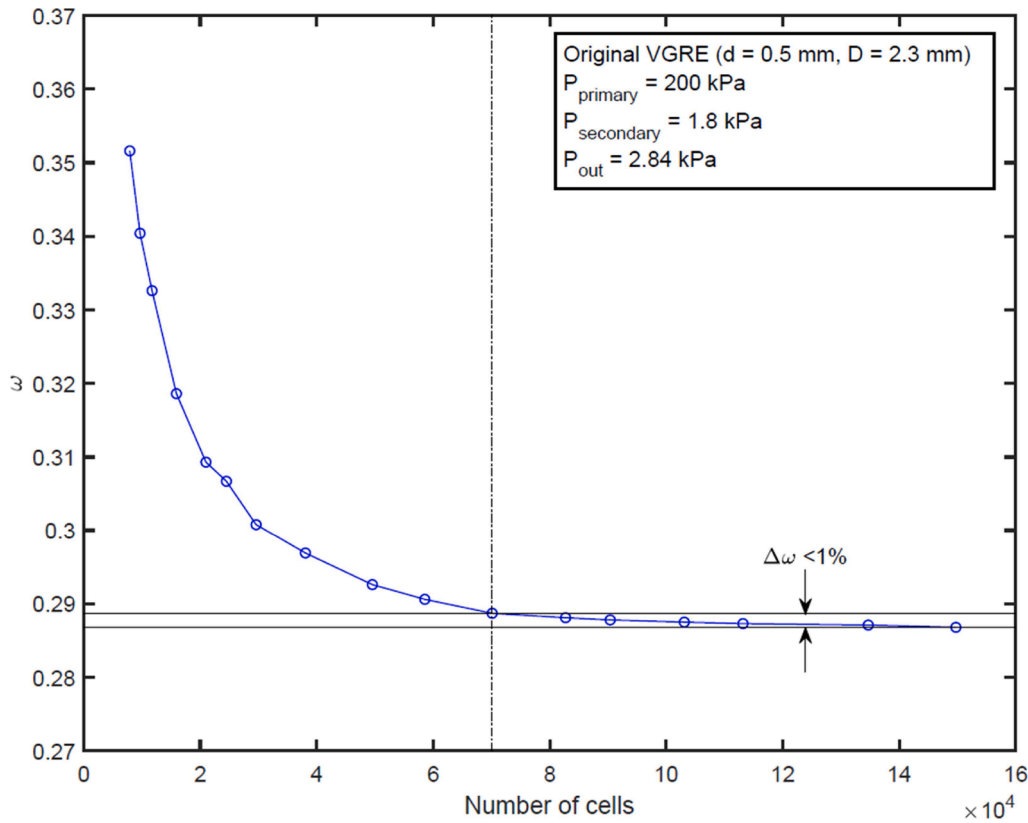


Fig. 3. Variation of ω with number of mesh cells using DES SST $k-\omega$ TM.

Table 2

Grid quality criteria.

Maximum aspect ratio	1.55
Y-plus value	< 0.60
Maximum skewness	0.41
Cell quality	> 0.90
Orthogonal quality	> 0.88

Inzoli [25] conducted a two-dimensional steady-state analysis of a supersonic axial ejector, employing seven distinct RANS-TMs. Their findings identified the SST $k-\omega$ model as achieving the closest alignment with experimental data across different ejector geometries and working conditions, with a maximum relative error of only 10 %. The recommendation to employ the SST $k-\omega$ model for simulating supersonic ejectors is supported by its tailored customization for accuracy in free-stream and near-wall regions, structural advantages, specific design for transonic to supersonic performance, and a proven track record. This recommendation is further reinforced by recent research from other investigators, highlighting the SST $k-\omega$ model's merit in simulating supersonic ejectors [36,37]. Despite the prevalence of RANS-TMs in prior numerical investigations of supersonic axial ejectors, there is a surprising lack of studies employing CFD analyses with Large Eddy Simulation (LES) or comparing RANS models against experimental data in both steady and transient states for radial ejectors.

The exploration of variable geometry radial ejectors (VGREs) and their performance involves the integration of machine learning (ML) and optimization techniques to compare CFD simulation results with experimental data. ML algorithms, rooted in regression analysis and neural networks, facilitate the development of predictive models capable of discerning intricate relationships among design parameters, flow conditions, and ejector performance metrics. Trained on experimental data, these models serve as potent tools for fine-tuning CFD

simulation inputs, achieving closer alignment with real-world experimental results [38]. Additionally, optimization techniques such as genetic algorithms and particle swarm optimization iteratively adjust simulation parameters to maximize agreement between CFD predictions and experimental observations [39,40]. This fusion of ML and optimization not only enhances the accuracy of CFD simulations but also expedites the design and optimization of VGRE configurations, advancing understanding of these complex systems. ML's benefit lies in its ability to construct models without awareness of the underlying physical principles, simplifying their construction compared to physics-based models [41]. Previous research using ML techniques has successfully characterized mathematical connections between input and output variables, improving analysis accuracy [42–46]. In ejector applications, where performance indicators may exhibit an inverse relationship, multi-objective optimization techniques might be employed to navigate the trade-off between these indicators, allowing for a more comprehensive understanding of ejector system performance under diverse conditions. Various ML techniques have been utilized to forecast ejector performance, encompassing decision trees [47,48], artificial neural networks [49,50], Gaussian process regression [51], and support vector machines [52]. These models serve as resilient alternatives for exploring intricate fluid processes within devices such as ejectors. The application of ML techniques in ejectors facilitates accurate predictions of both local and global performances, leveraging available experimental or numerical datasets.

The primary aim of this study is to enhance the design of a radial ejector, shifting away from a traditional reliance on extensive experimental investigations toward a more efficient and cost-effective approach that involves testing the new design using CFD software. Notably, within the literature, a consensus appears to exist regarding the effectiveness of the SST $k-\omega$ model in modeling axial ejectors. Yet, there is a conspicuous lack of consensus on the optimal CFD model for simulating radial ejectors. This knowledge gap regarding validation studies

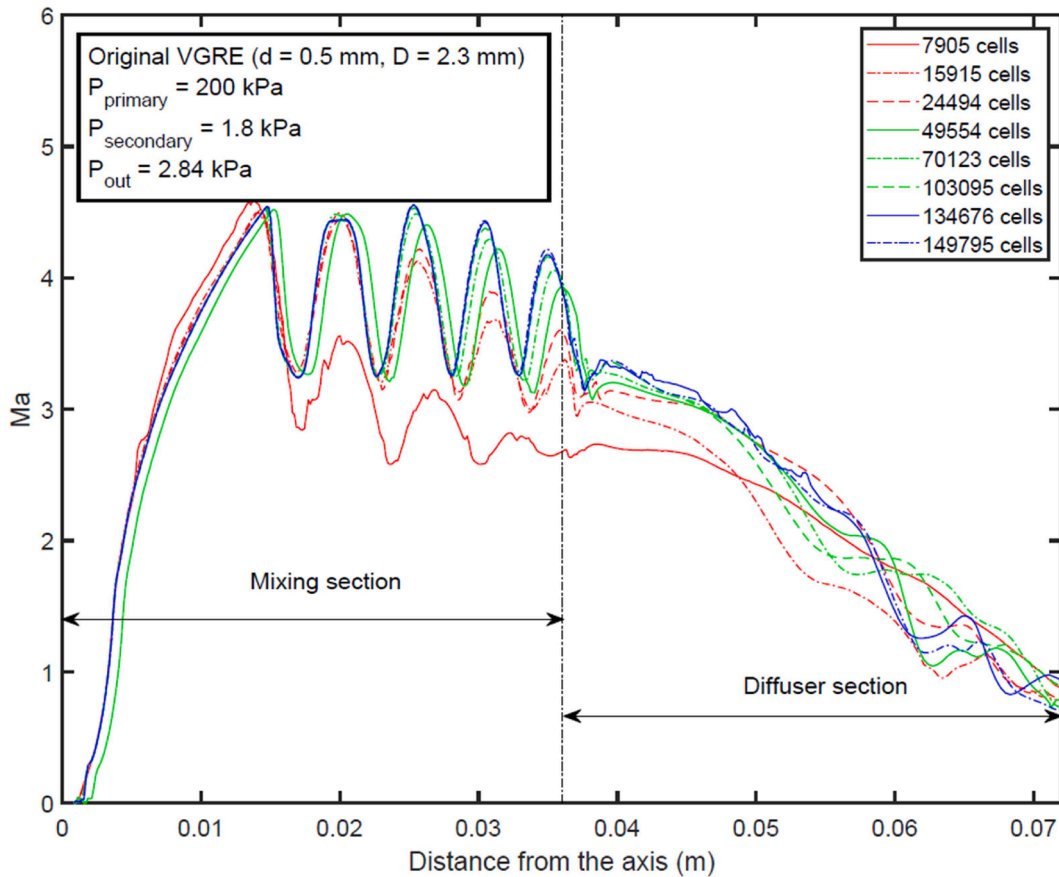


Fig. 4. Profiles of Ma along center-plane of improved VGRE for different number of mesh cells using DES SST $k-\omega$ TM.

Table 3

Original VGRE operation conditions specified in the simulations and experiments.

Boundary conditions	Pressure (kPa)	Temperature (K)
Primary stream	160, 200, 250, 270	300
Secondary stream	1.8, 2.5, 3.2	300
Outlet stream	2 to 7	300

for VGREs utilizing either RANS or detached eddy simulation (DES)-TMs serves as the driving force behind this research endeavor focused on the novel design of adjustable radial ejectors.

As a result, this study introduces innovative simulations of the original VGRE configuration, harnessing the capabilities of DES-TMs within the ANSYS FLUENT software platform. Subsequently, these simulations are thoroughly compared against available experimental data [15], all with the overarching objective of identifying the most suitable TM. This comparative analysis is conducted carefully to maintain consistency in geometry, working fluid, and operating conditions. The CFD simulations are carried out using ANSYS FLUENT 19.1 to assess the global ejector performance indicators, such as the entrainment ratio (ω), critical outlet pressure (P_{out}^*), critical compression ratio (r_c^*), and ejector efficiency (η) as the overall ejector performance. Meshing is fine-tuned to represent velocity gradients in critical regions accurately. Convergence criteria ensure solution accuracy. CFD investigations also emphasize capturing the boundary layer and mixing areas to evaluate the local ejector performance indicators based on Mach number (Ma) and wall static pressure (P_{static}). Another significant contribution to this study is employing the Gaussian Process Regression (GPR) approach as a supervised machine-learning technique and the Marine Predators Algorithm (MPA) approach as an optimization tool. In this turn, the

available datasets are initially utilized in a multi-output GPR model to predict the relationship between various factors and the corresponding responses. The next stage is carried out based on a multi-objective MPA optimization approach to maximize leading ejector performance indicators: (i) entrainment ratio (ω), (ii) critical compression ratio (r_c^*), and (iii) ejector efficiency (η).

2. Ejector performance

Critical outlet pressure (P_{out}^*) and entrainment ratio (ω) are commonly utilized performance indicators for evaluating ejector performance. The ω represents the ratio of secondary mass flow rate ($\dot{m}_{secondary}$) to primary mass flow rate ($\dot{m}_{primary}$), while the P_{out}^* is the pressure at which the ω begins to decline as the outlet pressure (P_{out}) increases. Higher values of ω and P_{out}^* typically indicate improved ejector performance. Additionally, ejector performance can also be characterized by the expansion ratio (r_e), which quantifies the ratio of primary flow pressure ($P_{primary}$) to secondary flow pressure ($P_{secondary}$), and the critical compression ratio (r_c^*), which represents the ratio of P_{out}^* to $P_{secondary}$. The ejector efficiency (η) is an important indicator that is often used for assessing the performance of ejectors. The overall performance, as evaluated by ejector efficiency, is a comprehensive indicator of ejector performance. This is because the ejector efficiency considers the values of the secondary and primary mass flow rates as well as the outlet, secondary, and primary pressures.

In this study, the primary nozzle and ejector duct plates were designed with disk-like surfaces that could be adjusted to modify the nozzle and ejector throat areas within a single ejector. The study aimed to investigate the impact of different nozzle throat separations (d) and duct throat separations (D), as shown in Fig. 1, across a broad range of operating conditions. The VGRE's operating principle and the main

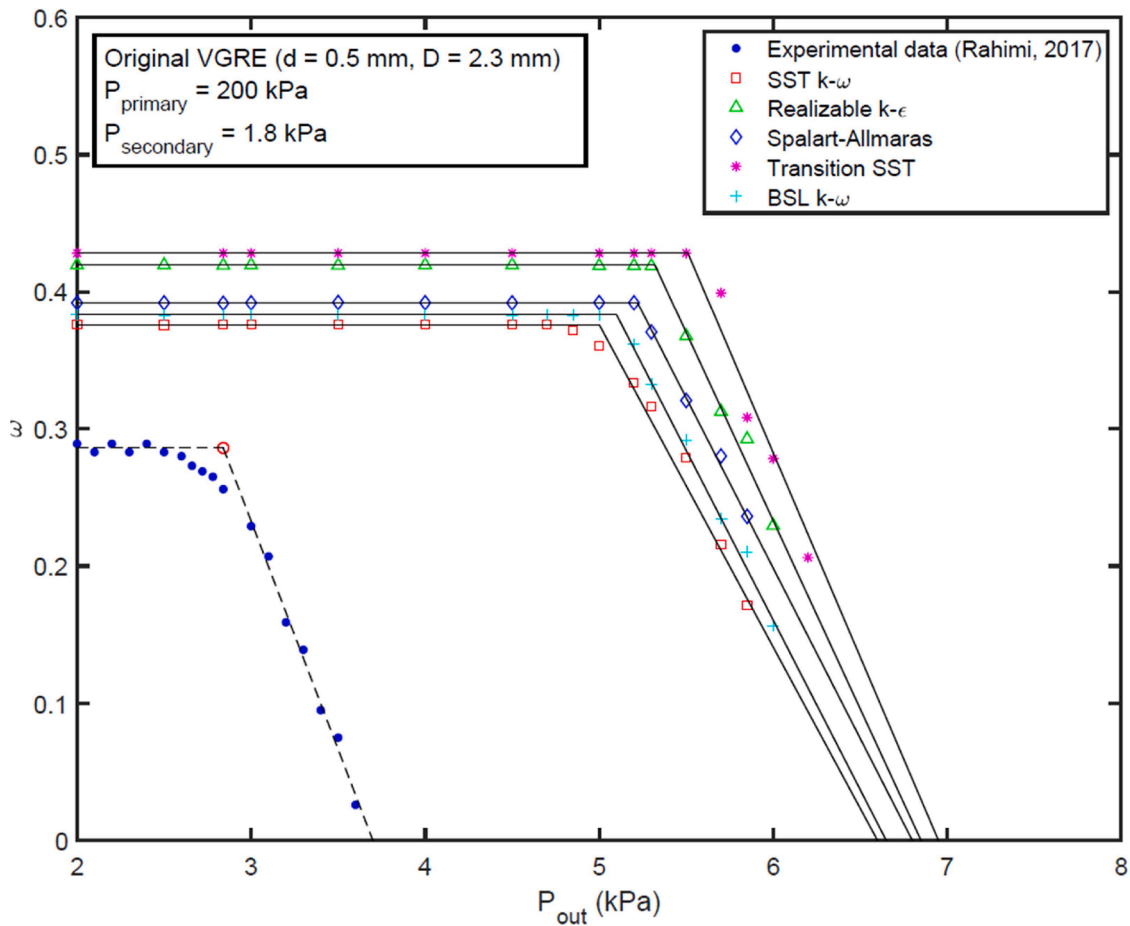


Fig. 5. Variation of ω with P_{out} for RANS-TMs.

equations representing the VGRE's performance have been stated and discussed in more detail in Ref. [53].

3. Configuration of CFD simulations

3.1. Detached eddy simulation (DES)

One of the primary challenges in effectively implementing the DES approach lies in determining the interface between the RANS and LES regions, which is contingent upon the grid spacing. To achieve a smooth transition from RANS to LES within the boundary layer, it is necessary to employ a fine mesh with significantly smaller grid spacing compared to the thickness of the boundary layer. The positive aspects of utilizing DES instead of RANS can be observed in two main aspects: (i) RANS models are proficient at handling boundary layers and their separation but struggle with large separation regimes; and (ii) time-resolved simulations, often advantageous for engineering analysis, particularly in areas such as noise and vibration. ANSYS FLUENT software offers several options for the DES-TMs: DES SST $k-\omega$, DES Realizable $k-\epsilon$, DES Transition SST, DES Spalart-Allmaras, and DES BSL $k-\omega$ [54]. These options offer flexibility and diverse capabilities for simulating turbulent flows using the DES approach. Hybrid RANS/LES methodologies offer promising possibilities to enhance the accuracy of predicting separated flows while maintaining reasonable computational time costs. DES models, specifically designed for handling separated flows and high Reynolds number wall-bounded flows, serve as an alternative when the computational time required for a near-wall resolving LES is prohibitive. In contrast to the LES model, DES relies solely on the necessary RANS resolution within the boundary layers. Although DES models have lower computational time costs compared to LES models, they still incur

higher costs than RANS models [55].

3.2. CFD configuration

The effectiveness analysis of the VGRE was conducted using ANSYS FLUENT 19.1. The CFD simulations utilized compressible axisymmetric 2-D models with air as the working fluid.

The density-based implicit solver method was utilized to solve the conservation equations, which included mass, momentum, and energy conservation, in an unsteady formulation. To ensure stability, a time step size of 5×10^{-6} s was selected after multiple iterations. The simulations were conducted over a duration of 10,000-time steps, with 150 iterations per time step reporting interval. This allowed for the collection of unsteady statistics for all the models [56]. Table 1 provides a comprehensive overview of the parameter settings utilized in the CFD FLUENT model for the RANS-TMs and DES-TMs.

3.3. Meshing approach

To capture significant gradients in regions such as the primary nozzle, mixing area, and near-wall regions, a fine mesh density was utilized by setting the mesh face sizing. In particular, the mixing regime and shock regimes required a fine mesh due to their substantial velocity gradient variations. The boundary layer was characterized with three layers of mesh inflation to ensure a Y^+ value below 0.6, as illustrated in Fig. 2. This meshing approach has been previously reported in several studies [25,56,57]. In the current simulations, a fine mesh was utilized, ensuring a minimum of 20 cells/mm in the transverse direction, with a maximum face size of 0.08 mm. This high-resolution mesh enabled an effective representation of the mixing regime, particularly in the free

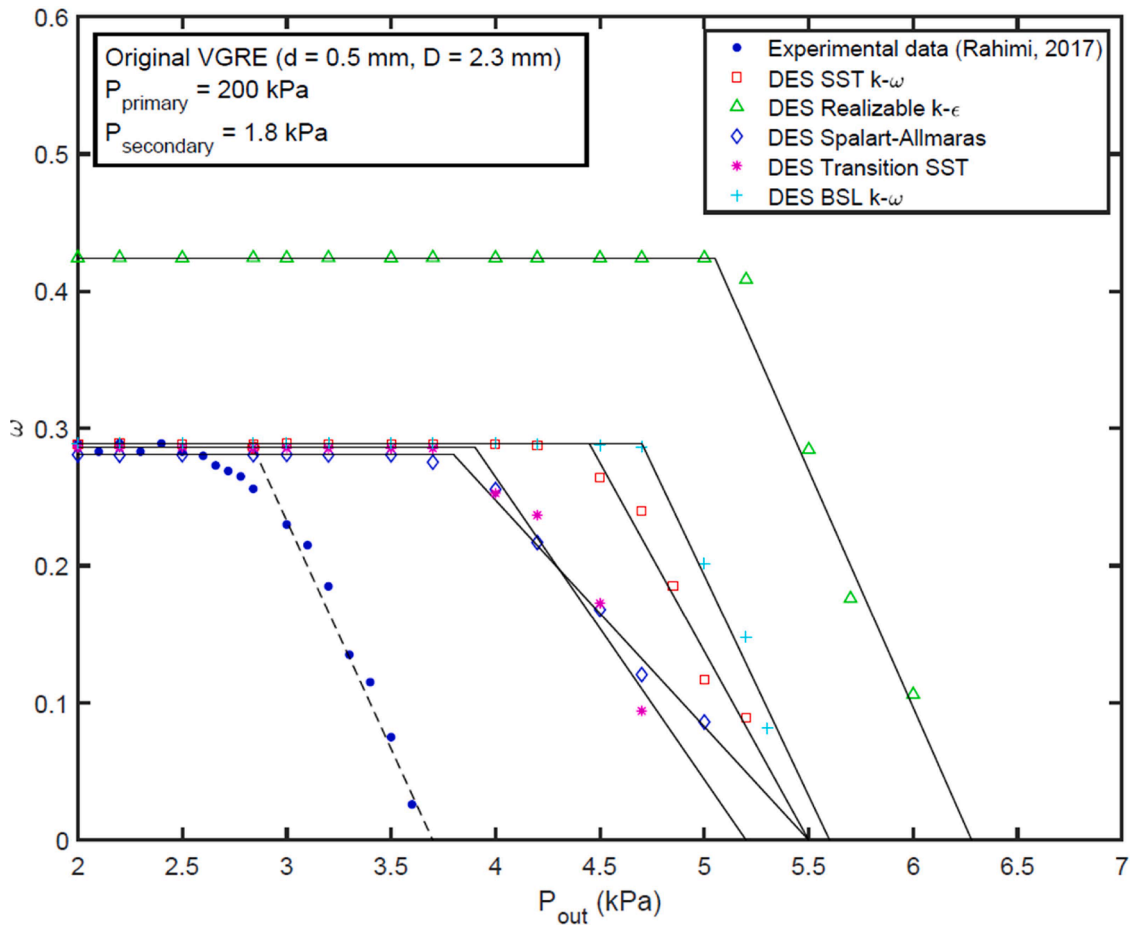


Fig. 6. Variation of ω with P_{out} for DES-TMs.

Table 4

Experimental and simulation results for the original VGRE from Fig. 5 and Fig. 6.

Model	ω - EXP	ω - CFD	Error	P_{out} (kPa) - EXP	P_{out} (kPa) - CFD	Error
RANS models						
SST $k-\omega$	0.29	0.376	29.7 %	2.84	5.00	76.1 %
Realizable $k-\epsilon$	0.29	0.420	44.8 %	2.84	5.32	87.3 %
Spalart-Allmaras	0.29	0.392	35.2 %	2.84	5.22	83.8 %
Transition SST	0.29	0.428	47.6 %	2.84	5.51	94.0 %
BSL $k-\omega$	0.29	0.383	32.1 %	2.84	5.10	79.6 %
DES models						
DES SST $k-\omega$	0.29	0.289	0.3 %	2.84	4.45	56.7 %
DES Realizable $k-\epsilon$	0.29	0.424	46.2 %	2.84	5.05	77.8 %
DES Spalart-Allmaras	0.29	0.281	3.1 %	2.84	3.80	33.8 %
DES Transition SST	0.29	0.286	1.4 %	2.84	3.90	37.3 %
DES BSL $k-\omega$	0.29	0.289	0.3 %	2.84	4.70	65.5 %

shear layer. In contrast, a previous CFD study conducted by Ariafar et al. [58] utilized a minimum of four cells per mm in the transverse direction.

To guarantee accurate solution results, the following convergence criteria were implemented: (a) the relative residuals were maintained at a stable level below 10^{-4} ; (b) the discrepancy in \dot{m} between the inlet and outlet was controlled to ensure it remained below a certain threshold of 10^{-6} kg/s; (c) the area-weighted average values for the $P_{primary}$ and $P_{secondary}$ remained constant, as recommended by Besagni et al. [59]. These convergence criteria were rigorously applied to guarantee the reliability and accuracy of the obtained solution.

3.4. Mesh independence

The outcomes of a mesh sensitivity analysis for the original VGRE

using DES SST $k-\omega$ are depicted in Fig. 3. The test was conducted under specific pressure conditions, with $P_{primary}$, $P_{secondary}$, and P_{out} of 200, 1.8, and 2.84 kPa, respectively. The simulations were performed with different mesh sizes ranging from 8000 to 150,000 cells, corresponding to cell sizes ranging from 0.50 to 0.03 mm. As depicted in Fig. 3, a distinct variation in ω can be observed with an increasing number of cells in the mesh, up to approximately 70,000 cells. Beyond this point, the variation in $\dot{m}_{primary}$, $\dot{m}_{secondary}$, and ω was less than 1 % with further increases in mesh size. Therefore, to optimize computational efficiency while preserving accuracy, the simulations were conducted utilizing a mesh consisting of approximately 70,000 to 85,000 cells, with each cell having a size of 0.06 mm. The discrepancy in the number of cells employed for the original VGRE arose due to variations in nozzle and duct throat separations. Table 2 provides the grid quality criterion for

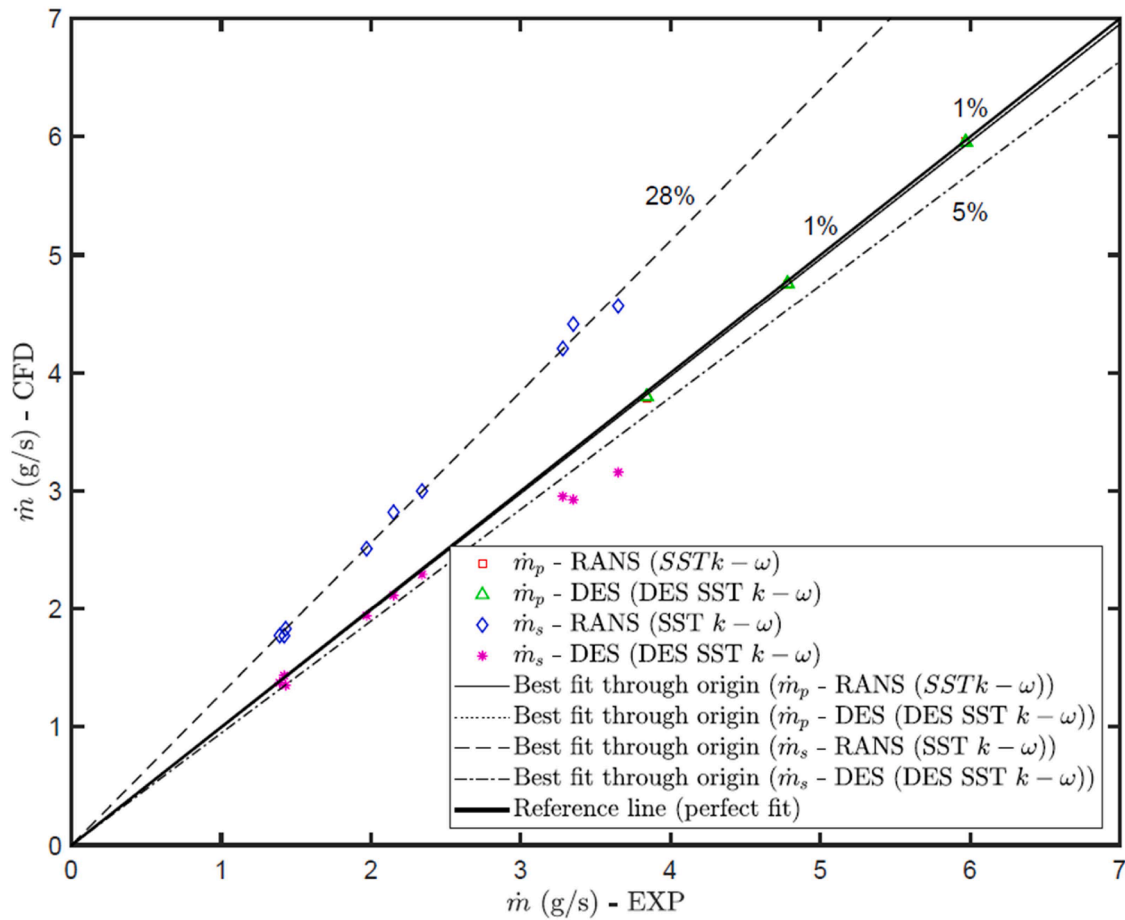


Fig. 7. Validation of \dot{m} with experimental results using RANS-TMs and DES-TMs.

the selected mesh cells ranging from 70,000 to 85,000.

The assessment of Mach number (Ma) distribution along the radial direction of the center-plane of the original VGRE was conducted in relation to the number of mesh cells, as displayed in Fig. 4. The Ma distribution was computed using DES SST $k-\omega$ for P_{primary} of 200 kPa, $P_{\text{secondary}}$ of 200 kPa, and P_{out} of 2.84 kPa. The simulations revealed a consistent amplitude of Ma variations in the mixing regime of the ejector for the number of mesh cells exceeding 70,000. Most of the diffuser section exhibited Ma greater than 1.0. As a result, the simulation outcomes may potentially lead to an overestimation of the P_{out}^* .

3.5. Assumptions and boundary conditions (BCs)

The current numerical simulations incorporate the following presumptions:

- The fluid flow within the ejector was treated as unsteady (transient flow).
- The walls of the ejector were considered to have a smooth surface, subject to no-slip BCs.
- The ejector walls were assumed to be adiabatic.
- The CFD simulations utilized compressible axisymmetric 2-D models with air as the working fluid (single-phase results).
- The BCs at the inlet and outlet were specified based on the stagnation state.
- The ejector wall's (wall thickness) domain was neglected.
- Equilibrium thermodynamics was postulated.

The numerical evaluation of the original VGRE was conducted in the current CFD investigation, considering various P_{primary} ranging from 160

to 270 kPa, $P_{\text{secondary}}$ ranging from 1.8 to 3.2 kPa, and P_{out} ranging from 2 to 7 kPa. The primary and secondary flow inlets were defined as "pressure inlet," while the mixed flow outlet was set as a "pressure outlet". The BCs at the inlet and outlet were specified based on the stagnation state, using values listed in Table 3. The BCs used in the CFD simulations were derived from the experimental tests conducted by Rahimi [15]. A comparison between the simulations and experiments was performed for the original VGRE, where air was utilized as the designated working fluid in the system, and the same geometry and operating conditions were applied in each scenario.

4. CFD models and validation

4.1. Validation of entrainment ratio (ω) and outlet pressure (P_{out})

The performance of radial ejectors was assessed by comparing RANS-TMs and DES-TMs. Fig. 5 illustrates the comparison between the experimental ω and the calculated ω obtained from the CFD model using different RANS-TMs. The CFD results revealed significant relative errors for the ω when employing RANS-TMs, ranging from approximately 30 % to 48 %. The lowest relative error, approximately 30 %, was observed with the SST $k-\omega$ model. The CFD results obtained using RANS-TMs exhibited inconsistency with the experimental data for choked flow (on-design operation) and unchoked flow (off-design operation) conditions across a variety of ejector operating conditions. This discrepancy could be attributed to the limited capability of RANS models in accurately simulating large separation regimes, despite their effectiveness in handling boundary layers and small areas of boundary layer separation. The surface quality at such small nozzle and duct throat separations may also contribute to differences between simulation results and

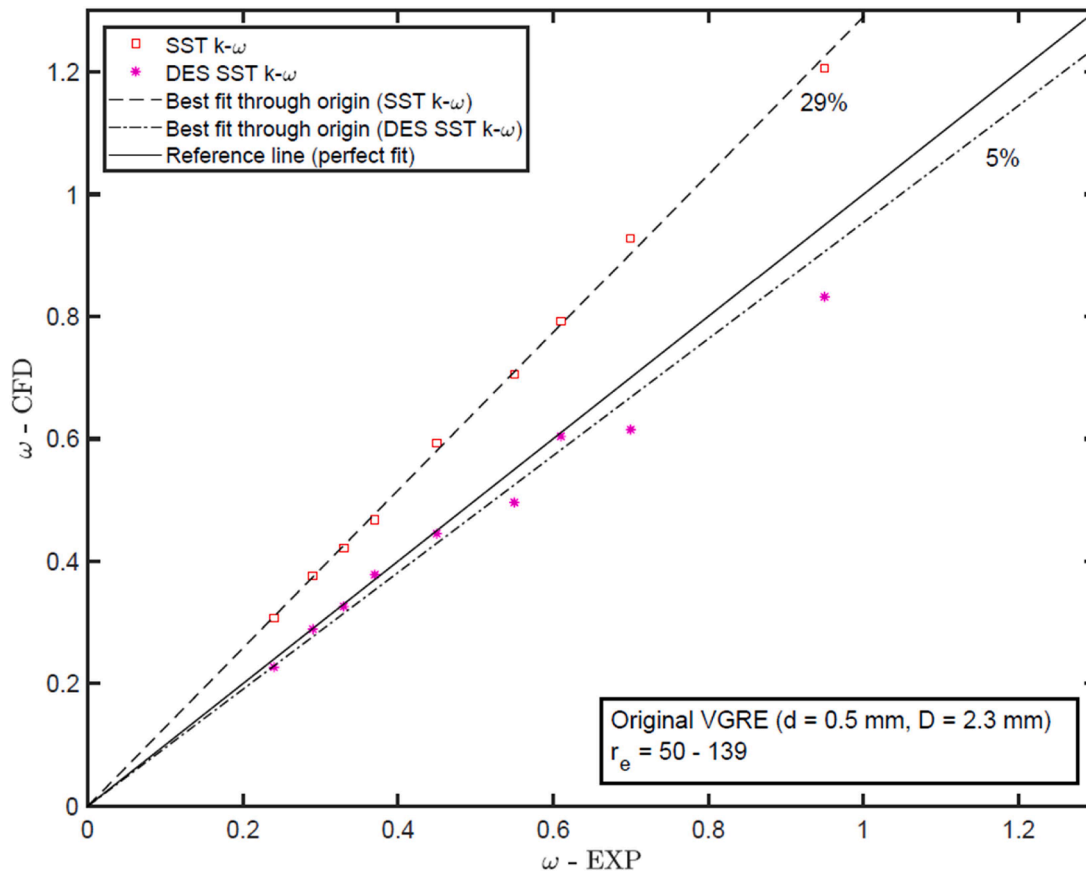


Fig. 8. Comparison of ω : CFD results vs. experimental data.

experiments. These factors highlight the importance of conducting geometry sensitivity assessments.

Fig. 6 showcases the comparison between the experimental ω and the corresponding values obtained from the CFD model utilizing different DES-TMs. The findings demonstrate the effectiveness of DES-TMs in accurately simulating the performance of the ejector with regard to ω during choked ejector operation, with acceptable errors consistent with those reported in the literature [25,32,60,61]. Among the DES-TMs, the maximum relative error for the ω was approximately 3 % for all models, except for DES Realizable $k-\epsilon$, which had a relative error of about 46 %. For the specified conditions, the ω obtained from the CFD results closely matched the experimental results, showing a relative error of less than 1 % for DES SST $k-\omega$. Consequently, the performance of radial ejectors was evaluated using the DES SST $k-\omega$ TM. However, in off-design conditions, the complexity increases as the entrainment of the secondary stream becomes highly dependent on the accuracy of the mixing simulations [29,32,57,61]. Consequently, larger discrepancies between the simulated and experimental results were observed during off-design operation. The proposed numerical approach employing DES models still struggles to accurately model the boundaries of the off-design model, which may be attributed to the design of the mixing section. Beyond the critical point (off-design condition), a 3-D model may yield more precise simulations of ejector performance relative to experimental data, as suggested by Mazzelli [32]. In Mazzelli's study, the 3-D simulations outperformed the 2-D simulations for off-design operation, with an average discrepancy of 13.9 % between 3-D simulations and experimental data, compared to an average discrepancy of 41.7 % between 2-D simulations and experimental data.

Table 4 provides an overview of the tested cases for the original VGRE, along with the corresponding models used and the related errors compared to the experimental data from Fig. 5 and Fig. 6. The evaluation of numerical results in this study was conducted by assessing the

relative error, which is defined according to Eq. (1).

$$Error(X) = \left| \frac{X_{EXP} - X_{CFD}}{X_{EXP}} \right| \times 100 \quad (1)$$

where X represents the variable being evaluated, X_{EXP} denotes the experimental measurement, and X_{CFD} represents the estimates obtained from the CFD model.

The simulation results based on CFD work by [15] indicated that the best RANS-TM for simulating the original VGRE performance was $k-\epsilon$ standard TM. The average discrepancy between the simulations and experimental results for the ω and P_{out}^* was found to be less than 16 % under on and off designs conditions [15]. However, in the present work, it should be noted that the SST $k-\omega$ TM demonstrated the best performance among the RANS-TMs used in simulating the original VGRE. At on-design conditions, the average discrepancy in terms of ω was approximately 30 %, indicating a relatively reasonable consistency. However, the SST $k-\omega$ TM showed poor performance in simulating the original VGRE at off-design operation. This discrepancy could be attributed to geometry differences between the experimental data from Rahimi [15] and the simulations. The components of the original VGRE were manufactured using 3-D printing, which introduces the possibility of deformation and deflection caused by mechanical loading or thermal effects. These factors can impact the tolerance and surface quality of the original VGRE, leading to variations between the simulated and experimental results.

4.2. Validation of mass flow rates (\dot{m})

Fig. 7 illustrates the comparison between the simulated and the experimental \dot{m} for both RANS-TMs and DES-TMs. A unity slope reference line is included to illustrate the deviation of the simulated results

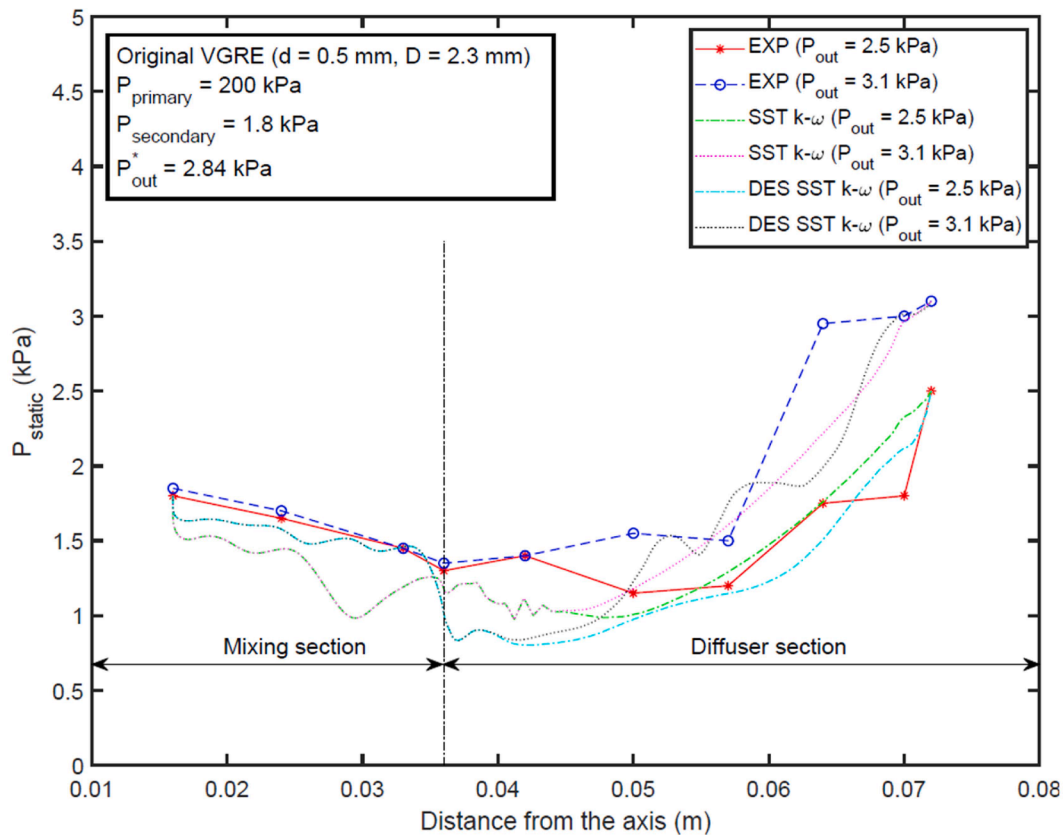


Fig. 9. Comparison of P_{static} distribution: SST $k-\omega$ vs. DES SST $k-\omega$ TMs.

from the experimental data. The outcomes show that the simulated $\dot{m}_{primary}$ closely matched the experimental data for both models. The average discrepancy between the experiments and the simulated $\dot{m}_{primary}$ was less than 1 % for both models. Consequently, the observed differences in the ω between the experiments and simulations in subsequent sections can be attributed to variations in the secondary flow rate. It is important to note that the experimental results for the SST $k-\omega$ TM exhibited an overestimation of the secondary flow rates, whereas the DES SST $k-\omega$ TM yielded improved consistent with the experimental data in predicting the secondary flow rates. The deviation between the experimental and simulated secondary flow rates was approximately 28 % when the SST $k-\omega$ model was utilized, while it reduced to around 5 % when the DES SST $k-\omega$ model was employed.

4.3. Validation of entrainment ratio

Fig. 8 presents a comparison between the experimental ω and the ω obtained from the CFD simulations using the SST $k-\omega$ and DES SST $k-\omega$ models. The CFD outcomes reveal that the errors in the simulated ω relative to the experimental data varied depending on the expansion ratio, ranging from 50 to 139. For the SST $k-\omega$ model, the errors were approximately 29 %, while for the DES SST $k-\omega$ model, the errors were reduced to around 5 %.

4.4. Validation of wall static pressure (P_{static})

Fig. 9 illustrates the profile of P_{static} along the walls of the ejector duct, showcasing the variations under both choked and unchoked flow conditions. The simulations were conducted utilizing the SST $k-\omega$ and DES SST $k-\omega$ TMs. The $P_{primary}$ was set to 200 kPa, the $P_{secondary}$ to 1.8 kPa, and two different P_{out} values were considered: 2.5 kPa (representing on-design operation) and 3.1 kPa (representing off-design operation). The results clearly demonstrate that the DES SST $k-\omega$ TM

yields more consistent results when compared to the experimental data for both choked and unchoked conditions in the mixing section. In contrast, the SST $k-\omega$ TM shows some deviations from the experimental data. However, the deviation from experimental data was observed for both TMs in both choked and unchoked conditions within the diffuser section. Particularly, the consistency between the simulation outcomes and experimental data was poor for the unchoked condition in the diffuser section. In this scenario, both TMs underestimated the experimental wall P_{static} .

The reduced entrainment of secondary flow into the mixing regime in the unchoked condition likely contributed to this discrepancy, leading to a decrease in the ω . The average discrepancy between the experimental and simulated wall P_{static} was approximately 9 % for on-design operation and about 10 % for off-design operation using the SST $k-\omega$ TM. Similarly, for the DES SST $k-\omega$ model, the average discrepancy was approximately 9 % for on-design operation and about 12 % for off-design operation.

The steady-state simulations, although providing valuable insights, may not capture asymmetries in the flow that could potentially contribute to the reduced secondary flow. Both TMs exhibit poor performance in simulating the experimental P_{static} at off-design operation. These discrepancies could be attributed to the presence of shock phenomena, which introduce complex flow behaviours in the unchoked state, leading to unexpected experimental outcomes. Additionally, it is noteworthy that the P_{static} measurements were only taken on the upper ejector duct plate. It is possible that the mixing between the primary and secondary streams was less complete during the experiments. Unfortunately, no additional data was available to support further analysis in this regard. Considering the available information from Rahimi's [15] experiments, the current simulations demonstrate that DES SST $k-\omega$ outperforms SST $k-\omega$ in both on and off design configurations.

While none of the CFD-TMs in the RANS and DES categories demonstrated satisfactory consistent with Rahimi's experimental data at

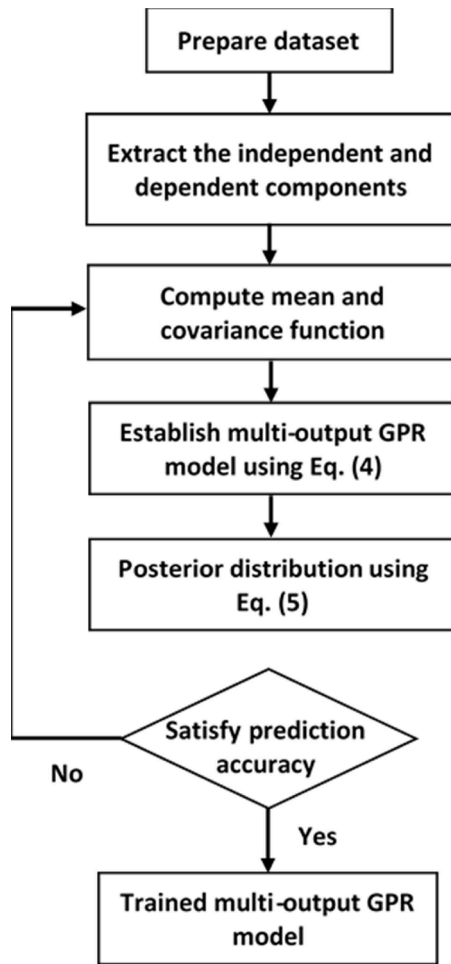


Fig. 10. Multi-output GPR model structure.

off-design conditions, the DES SST $k-\omega$ TM displayed improved consistency with the experimental data in both choked and unchoked conditions within the mixing section, compared to the SST $k-\omega$ TM. Moreover, as previously mentioned, the DES SST $k-\omega$ TM exhibited the closest alignment with the experimental data for the overall performance parameters. These findings reinforce the selection of the DES SST $k-\omega$ TM for future simulations of radial ejectors.

5. Machine learning (ML) approach and optimization algorithm

5.1. Machine learning (ML) approach: gaussian process regression (GPR)

The Gaussian process regression (GPR) model is a machine learning (ML) approach that operates within the Bayesian framework [62]. Depending on the number of model outputs, GPR models can be categorized as either single-output GPR or multiple-output GPR. A single-output GPR model comprises a finite set of independent variables, all variables drawn from a common Gaussian distribution. These variables are entirely determined by their means and covariance functions, as exemplified by Eq. (2) depicting the GPR definition.

$$f(x) \sim GPR(\mu(x), \sigma(x, x')) \quad (2)$$

Where x and x' represent two separate input samples, $\mu(x)$ is the mean function, typically assumed to be zero (without affecting the generalization and learning capabilities of the Gaussian Process). Additionally, $\sigma(x, x')$ stands for the covariance function of the Gaussian Process, which characterizes the correlation between independent variables.

The posterior distribution for the expected value y' can be computed

through the application of Bayesian theory, as demonstrated in Eq. (3):

$$p(y'|x, y, x') = N(\mu', \sigma'^2) \quad (3)$$

Where the input and output of the training set are denoted by x and y , while the input and prediction of the testing set are represented by x' and y' , respectively. The predicted mean is expressed as μ' , and the predicted covariance is indicated as σ'^2 .

The multi-output GPR model is formed by expanding upon the single-output GPR model. It addresses the limitation of the single-output GPR model, which cannot account for potential correlations among multiple outputs and necessitates the independent representation of each output. The multi-output GPR constructs a covariance matrix for each output to assess the correlations between individual outputs. It operates under the assumption that the various outputs are interconnected to some extent and leverages mutual information to generate more accurate predictions than those produced by the single-output GPR model [63].

The multi-output GPR suggests that any function within the set of T functions, $\{f_t(x)\}_{t=1}^T$, can be expressed as the convolution of the underlying function $\mu(x)$ with the smooth kernel function $\{G_t(x)\}_{t=1}^T$ $T=1$, as illustrated in Eq. (4):

$$f_t(x) = \int_x G_t(x-z)\mu(z)dz \quad (4)$$

Eq. (5) establishes the framework for the multiple-output regression problem:

$$y_t(x) = f_t(x) + \varepsilon_t \quad (5)$$

Where ε_t represents Gaussian noise, and y_t denotes multi-output function. Eq. (6) is employed to articulate the posterior distribution of the forecasted values y'_t in the framework of the multi-output GPR, following Bayesian principles.

$$p(y'_t|x, y, x') = N(\mu'_t, \sigma'^2_t) \quad (6)$$

A flowchart of the multi-output GPR model is illustrated in Fig. 10.

5.2. Optimization algorithm: marine predators algorithm (MPA)

A recent, simple, and highly effective metaheuristic optimization technique is known as MPA [64]. In a manner consistent with most other optimization techniques, MPA is a population-based metaheuristic method, generating the initial random solution using Eq. (7):

$$l_0 = l_{min} + rand(l_{max} - l_{min}) \quad (7)$$

Where "rand" refers to a uniform random vector sampled within the range of 0 to 1, while l_{min} and l_{max} represent the lower and upper bounds of the variables, respectively.

Following the principle of natural selection, which favors the fittest individuals, there is a common belief that apex predators in the natural world exhibit superior foraging skills. Consequently, the most proficient solution is referred to as the "apex predator" and is responsible for constructing a matrix referred to as "Elite," as demonstrated in Eq. (8). The arrays within this matrix are dedicated to monitoring and locating prey by utilizing information about their positions.

$$Elite\ Matrix = \begin{bmatrix} l_{1,1}^1 & \dots & l_{1,d}^1 \\ \vdots & \ddots & \vdots \\ l_{n,1}^1 & \dots & l_{n,d}^1 \end{bmatrix}_{n \times d} \quad (8)$$

The Elite matrix (EM) is established by replicating the top predator vector (\vec{l}) n times, where n corresponds to the number of search agents, and d represents the number of dimensions involved. Both predators and prey are classified as search agents because predators pursue their prey

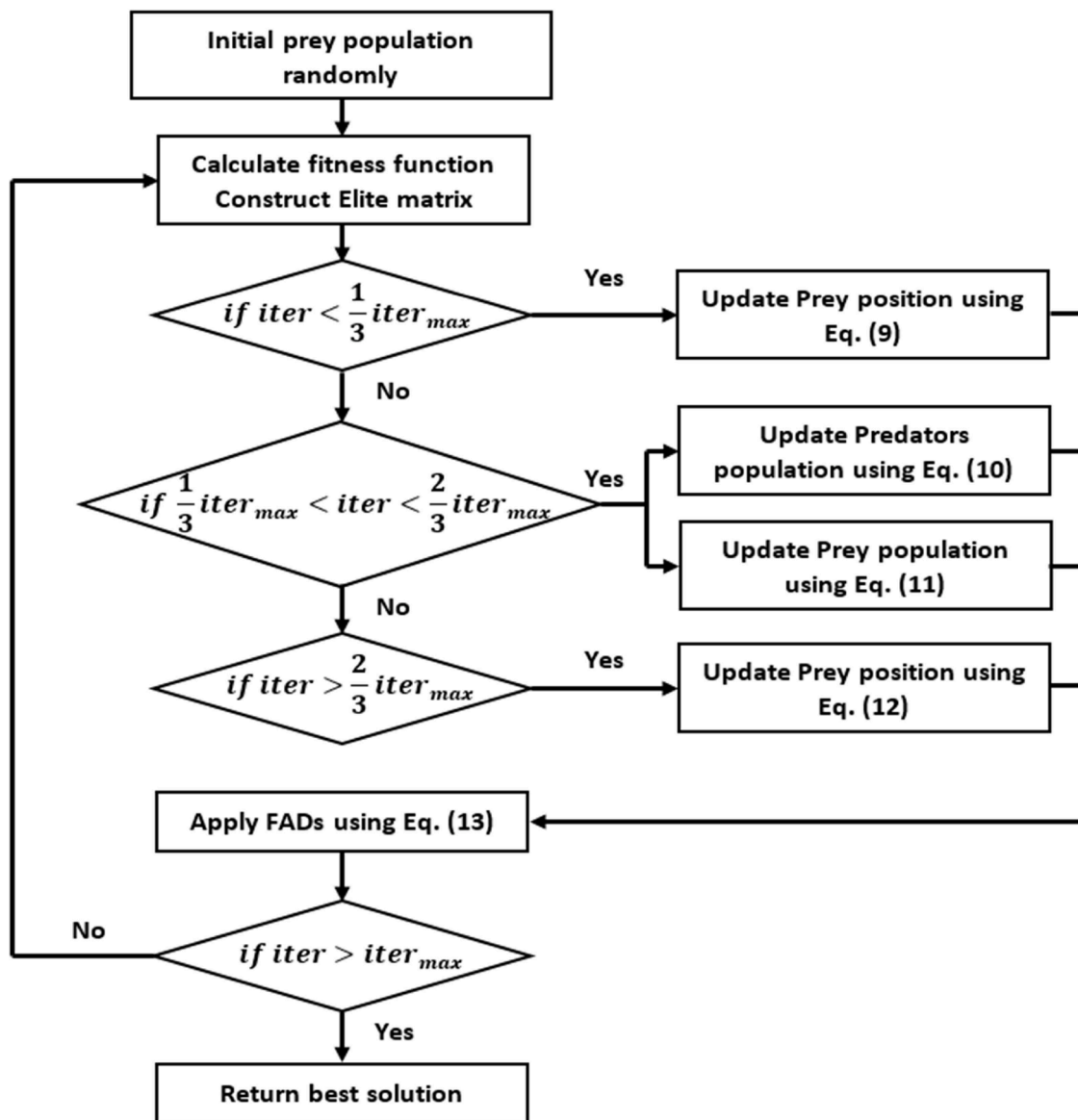


Fig. 11. MPA optimizer flowchart.

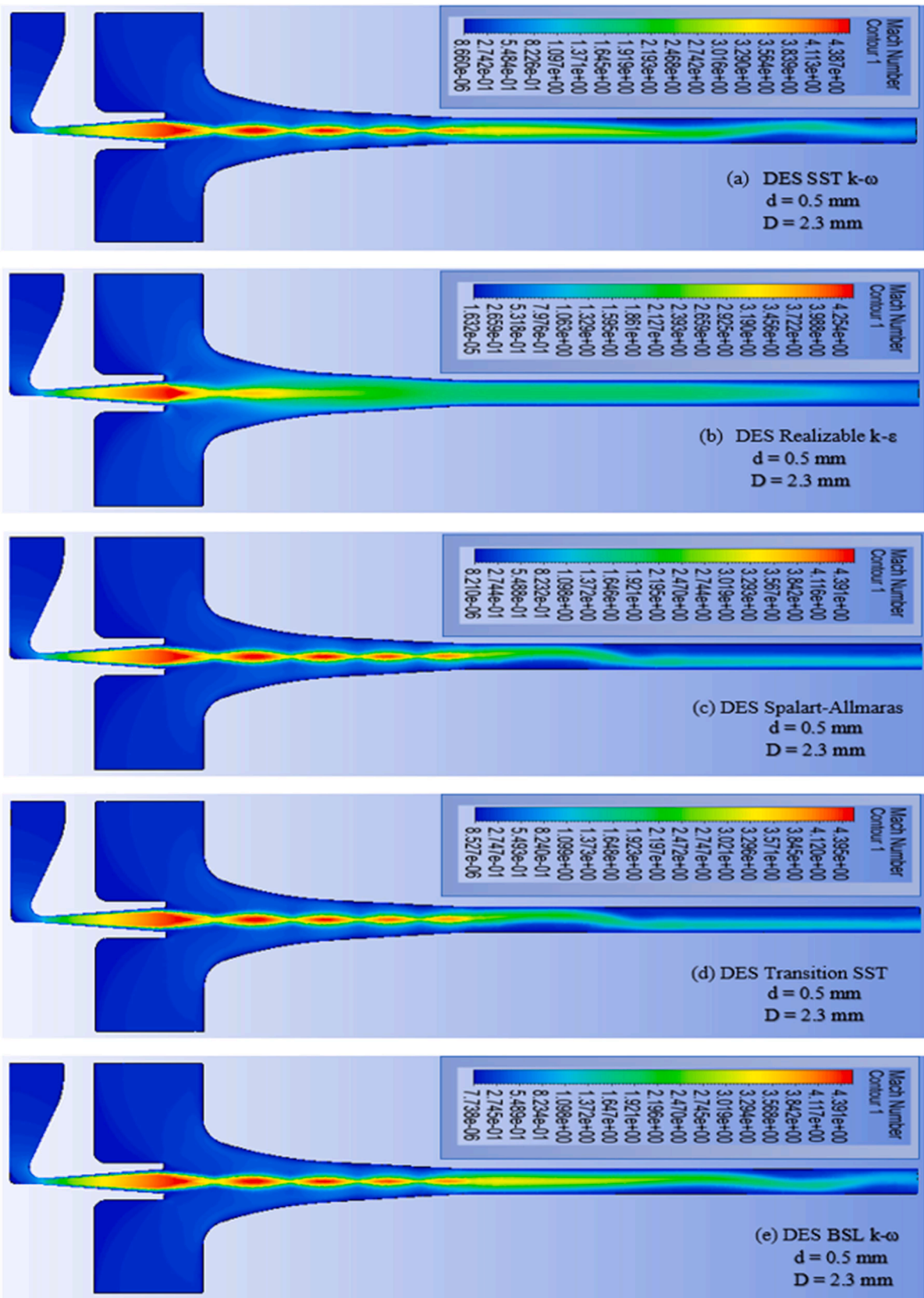


Fig. 12. Contours of Ma for DES-TMs.

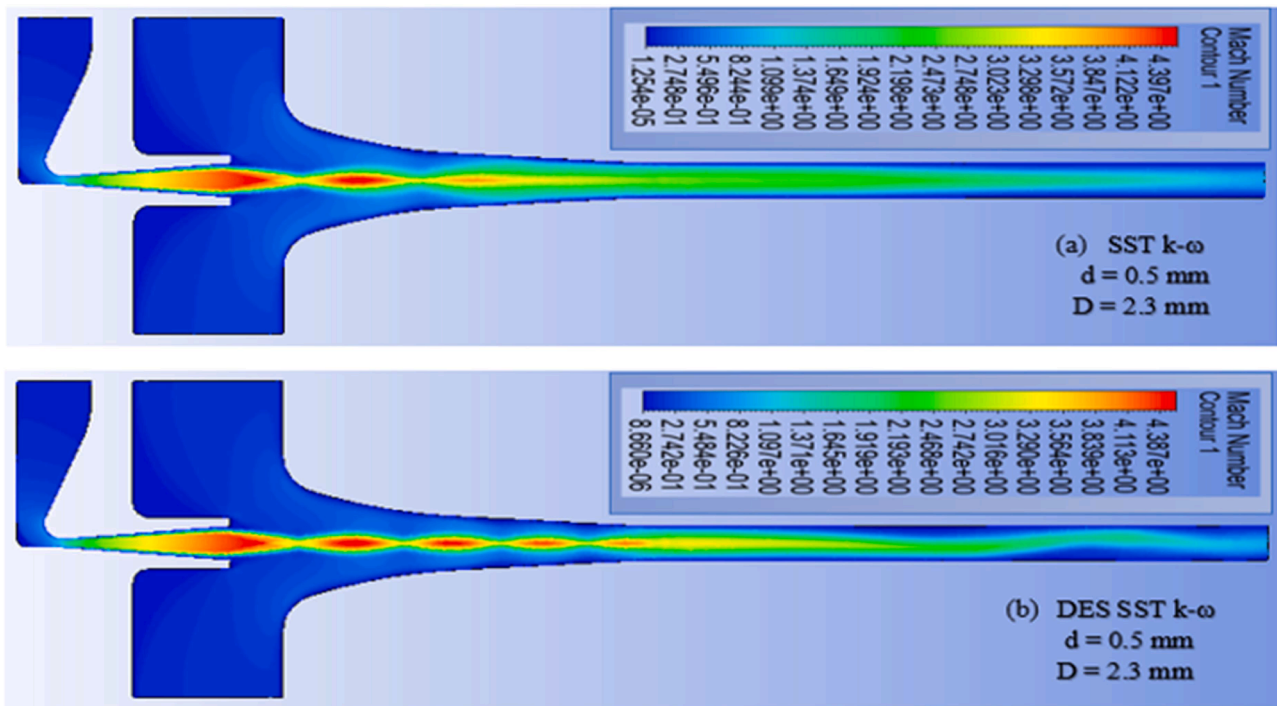


Fig. 13. Contours of Ma for the SST $k-\omega$ and DES SST $k-\omega$ TMs.

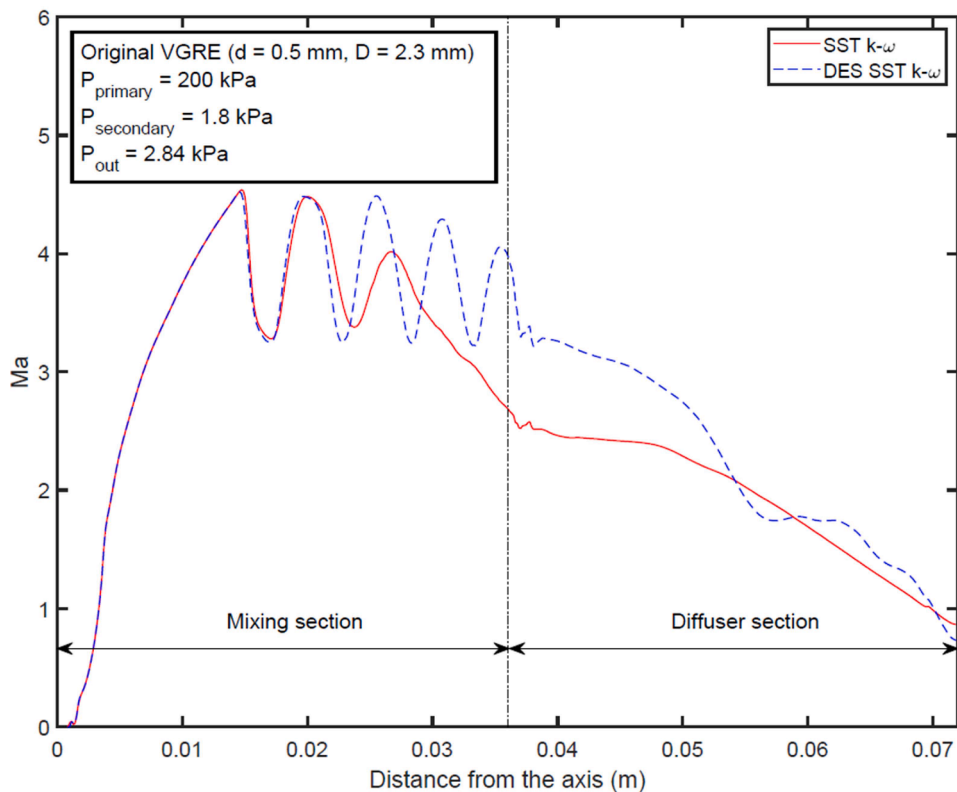


Fig. 14. Profiles of Ma along the center-plane of the original VGRE for the different TMs.

while the prey simultaneously searches for sustenance. Following each iteration, the EM undergoes updates if a superior predator displaces the current top predator. Another matrix, with the same dimensions as the EM, is known as the "prey matrix" (PM). Predators adjust their positions based on information from the PM. In simpler terms, the initialization

process begins by generating the initial PM, from which the most capable predator forms the EM. These EM and PM matrices play a pivotal role in the entire optimization process.

The optimization process of MPA is divided into three main stages, each considering different velocity ratios and simultaneously mimicking

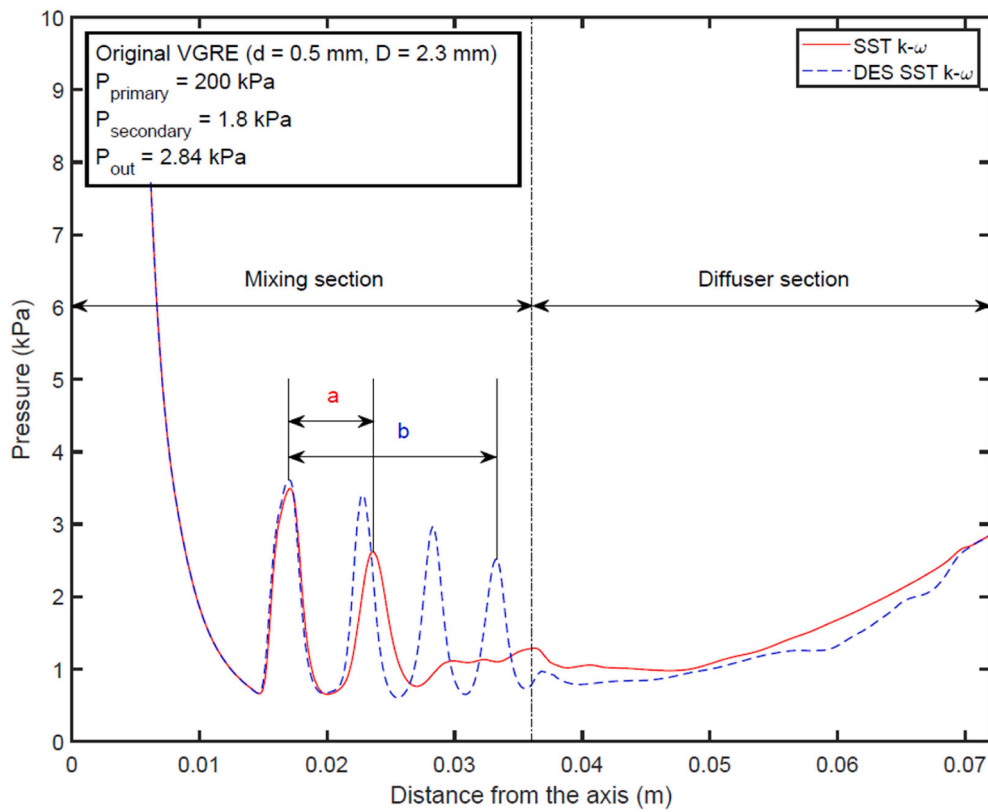


Fig. 15. center-plane pressure from CFD simulations for different TMs.

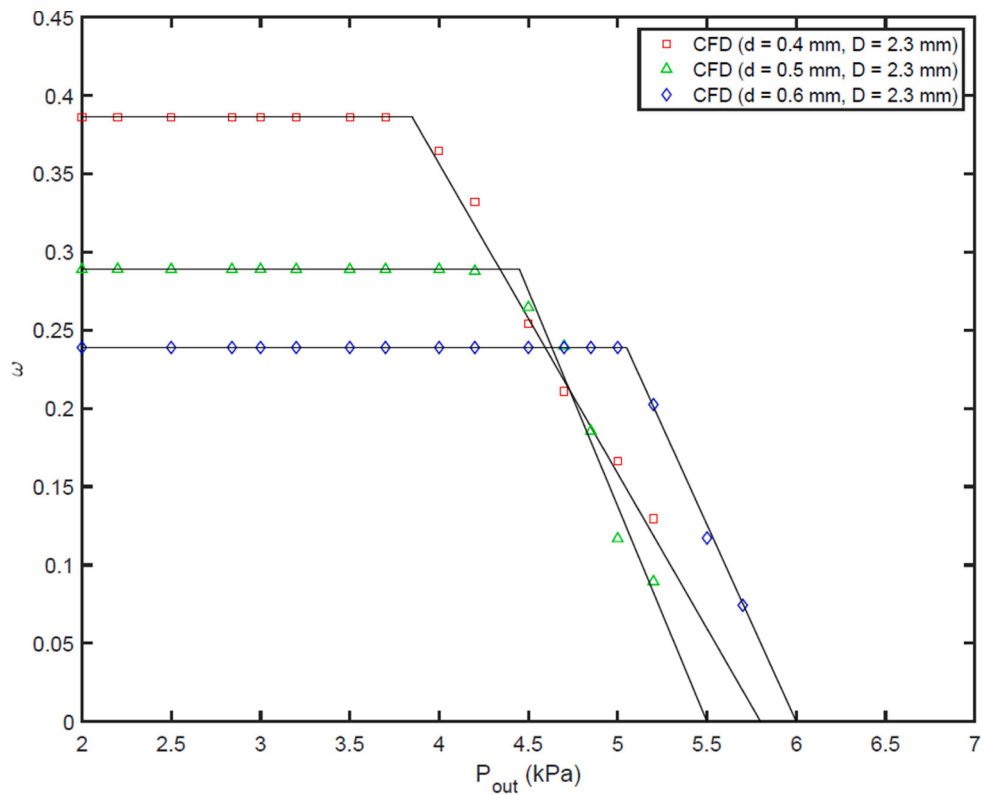


Fig. 16. Effect of d on ejector performance.

the complete lifecycle of both predators and prey. These stages are outlined as follows [64,65]:

Stage 1 (The first third of the iteration) commences when a high velocity ratio exists, indicating that the predator is moving faster than the prey. This phase predominantly occurs during the early iterations of the optimization process, focusing on exploration. In this phase, the optimal strategy for a predator is to remain stationary. This scenario can be mathematically expressed in Eq. (9):

$$\vec{PM}_i = \vec{PM}_i + a \cdot \vec{R} \otimes \overrightarrow{stepsize}_i \text{ where } \overrightarrow{stepsize}_i = \vec{R}_B \otimes (\vec{EM}_i - \vec{R}_B \otimes \vec{PM}_i) \quad i = 1, \dots, n \tag{9}$$

Where R_B is a vector signifying the Brownian motion and comprises randomly generated values from a normal distribution. The symbol \otimes denotes entry-wise multiplications. The multiplication of R_B by PM simulates the movement of prey. R represents a vector of uniformly distributed random values within the range [0, 1], while a is a constant

$$\vec{PM}_i = \vec{EM}_i + a \cdot CF \otimes \overrightarrow{stepsize}_i \text{ where } \overrightarrow{stepsize}_i = \vec{R}_L \otimes (\vec{R}_L \otimes \vec{EM}_i - \vec{PM}_i) \quad i = 1, \dots, n \tag{12}$$

with a value of 0.5.

Stage 2 (The second third of the iteration) starts when both the predator and prey are moving at the same speed, indicating a unit velocity ratio. This stage simulates the hunt of prey by both predators and prey. It takes place during the middle of the optimization process, where there is a brief transition from exploration to exploitation. This phase emphasizes the significance of both exploration and exploitation. The population is then divided into two halves for exploration and exploitation purposes, as delineated in Eq. (10) and (11) respectively. Predators assume the role of exploration, while prey concentrates on exploitation. According to the established rule, prey and predator are assigned Lévy and Brownian movements during this phase, respectively.

$$\vec{PM}_i = \vec{PM}_i + a \cdot \vec{R} \otimes \overrightarrow{stepsize}_i \text{ where } \overrightarrow{stepsize}_i = \vec{R}_L \otimes (\vec{EM}_i - \vec{R}_L \otimes \vec{PM}_i) \quad i = 1, \dots, \frac{n}{2} \tag{10}$$

$$\vec{PM}_i = \vec{EM}_i + a \cdot CF \otimes \overrightarrow{stepsize}_i \text{ where } \overrightarrow{stepsize}_i = \vec{R}_B \otimes (\vec{R}_B \otimes \vec{EM}_i - \vec{PM}_i) \quad i = \frac{n}{2}, \dots, n \tag{11}$$

Where R_L represents a vector of random values that corresponds to the

$$\vec{PM}_i = \vec{EM}_i + a \cdot CF \otimes \overrightarrow{stepsize}_i \text{ where } \overrightarrow{stepsize}_i = \vec{R}_L \otimes (\vec{R}_L \otimes \vec{EM}_i - \vec{PM}_i) \quad i = 1, \dots, n \tag{13}$$

Lévy movement, derived from the Lévy distribution. Prey movement is simulated using a Lévy approach through the multiplication of R_L and PM , while prey movement involves adding the step size to the prey

location. This part contributes to exploitation since most of the Lévy distribution step sizes are associated with small steps. While the convergence factor (CF) serves as an adaptive parameter controlling the step size of predator movement. Prey adjusts its position based on predator movement using Brownian motion, where R_B and EM are multiplied together to replicate the predator's movement in Brownian motion.

Stage 3 (The last third of the iteration) commences when a predator

moves faster than a prey or when a low velocity ratio is observed. This situation occurs during the concluding phase of optimization, often associated with a heightened exploitation capacity. In this stage, the optimal strategy for a predator is to engage in the Lévy movement to ensure enhanced exploitation capability. Eq. (12) exemplifies this stage:

In the Lévy method, the movement of the predator is mimicked by multiplying R_L and EM . Additionally, enhancing the Elite position with the step size facilitates the predator's motion, contributing to updating the prey's position.

Environmental factors, such as the formation of eddies or the presence of Fish Aggregating Devices (FADs), can influence the behavior of marine predators. As indicated by Filmalter et al. [66], sharks allocate over 80 % of their time in the proximity of FADs, reserving the remaining 20 % for exploring other potential prey distributions, often accomplished through longer leaps. FADs are perceived as traps representing local optimal solutions. These extended leaps serve to prevent entrapment in local stagnation. Consequently, the mathematical repre-

sentation of the impact of FADs is encapsulated in Eq. (13).

Where the likelihood of FADs influencing the optimization process is 0.2. The vector \vec{U} is a binary, comprising arrays of zero and one. This is achieved by generating a random vector within the range [0, 1] and

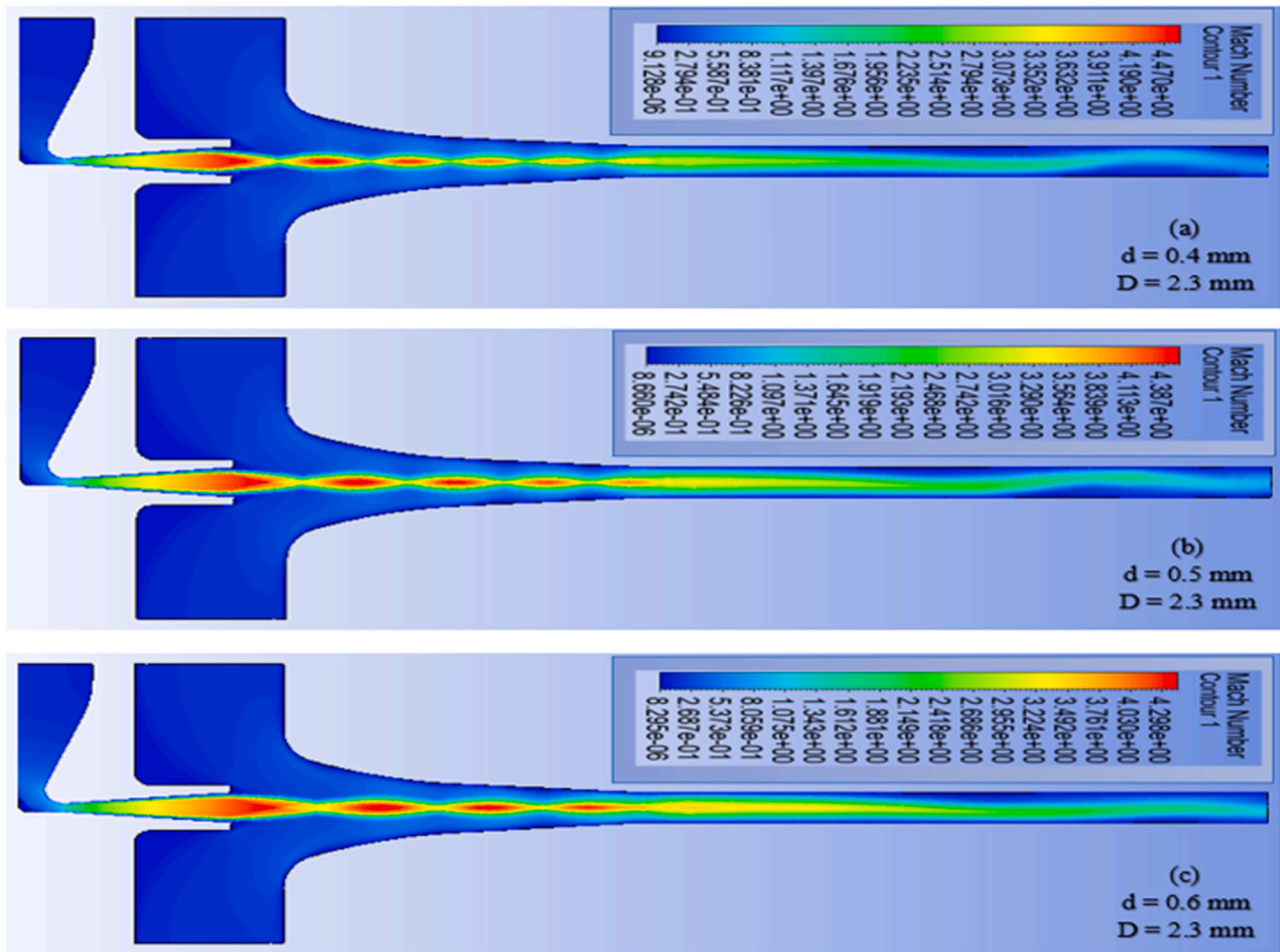


Fig. 17. Contours of Ma for different d values at an P_{out} of 2.84 kPa.

assigning zero to its element if it is less than 0.2, or one if it is greater than 0.2. The random number between 0 and 1 is represented as 'r'. The vectors l_{min} and l_{max} encompass the lower and upper boundaries of the dimensions. The subscripts r_1 and r_2 denote the random indexes for the PM.

The PMA exhibit an impressive ability for remembering locations where they have previously found food successfully. In the MPA approach, this capability is replicated through a memory-saving mechanism. After updating the prey distribution and considering the influence of FADs, the matrix representing these experiences is assessed for its effectiveness in updating the EM. The fitness of each solution in the current iteration is compared to its counterpart from the previous iteration. If the current solution proves superior, it replaces the previous one. This iterative process not only improves the quality of solutions over time but also encourages predators to revisit areas where successful hunting occurred. The flowchart of MAP step-by-step procedure is shown in Fig. 11.

6. Results and discussion

6.1. Mach number (Ma) and static pressure (P_{static})

Fig. 12 demonstrates the Ma contours of the original VGRE obtained using various DES-TMs: DES SST k- ω , DES Realizable k- ϵ , DES Spalart-Allmaras, DES Transition SST, and DES BSL k- ω . The simulations revealed that the maximum Ma ranged from approximately 4.25 to 4.40 for the different models, with DES Realizable k- ϵ exhibiting a slightly

lower maximum Ma . However, upon comparing the Ma contours of the different models, notable differences in shock and expansion structures within the free jet regime can be observed. These variations in shock phenomena and mixing processes could contribute to the higher Ma at the exit section of the mixing chamber in the DES-TMs, potentially explaining the higher simulated P_{out}^* compared to the experimental data. Additionally, the Ma contours indicate that the shock and expansion structures shifted upstream in the DES Realizable k- ϵ model due to a slight decrease in Ma relative to the other DES-TMs. However, it is worth noting that DES Realizable k- ϵ consistently yielded higher ω and P_{out}^* compared to the other DES-TMs. These observed differences could be attributed to the relatively lower intensity of waves evident in the DES Realizable k- ϵ model in comparison to the other DES-TMs.

Regarding the ω , the simulation results indicated that the SST k- ω model demonstrated the highest level of matching among the RANS-TMs, while the DES SST k- ω model exhibited the best performance among the DES-TMs when compared to the experimental data. Fig. 13 presents the Ma contours of the original VGRE derived using the RANS and DES models with the SST k- ω TM. The maximum Ma observed was around 4.4 for both models. However, significant differences were observed in the shock and expansion structures between the DES SST k- ω simulations and the SST k- ω simulations. The relative errors for the ω , when compared to the experimental data, were approximately 30 % for the SST k- ω model and 1 % for the DES SST k- ω model. The DES SST k- ω model exhibited less symmetric flow behavior along the center-plane of the ejector contrast with the SST k- ω model. This asymmetry could be

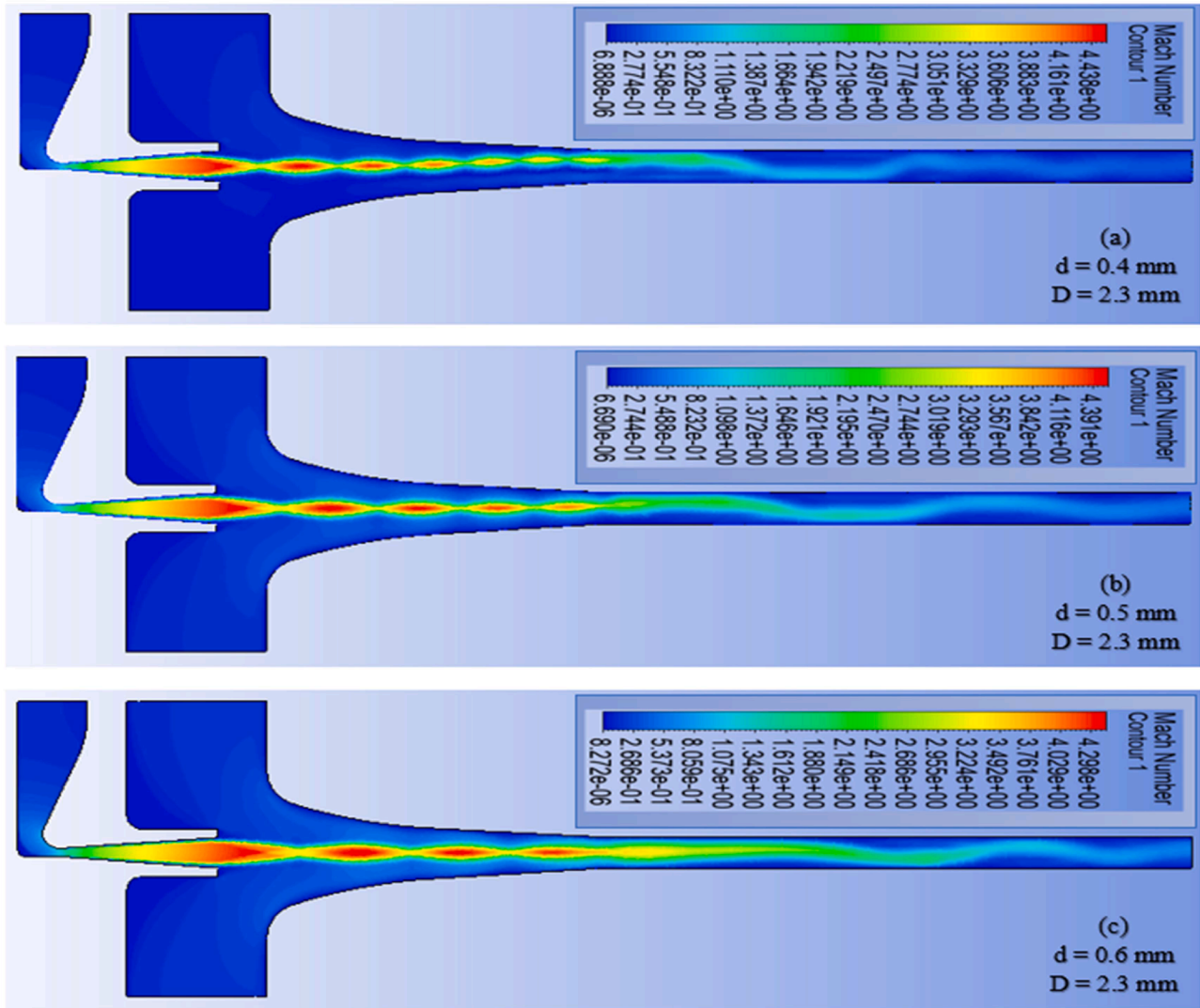


Fig. 18. Contours of Ma for different d values at an P_{out} of 4.5 kPa.

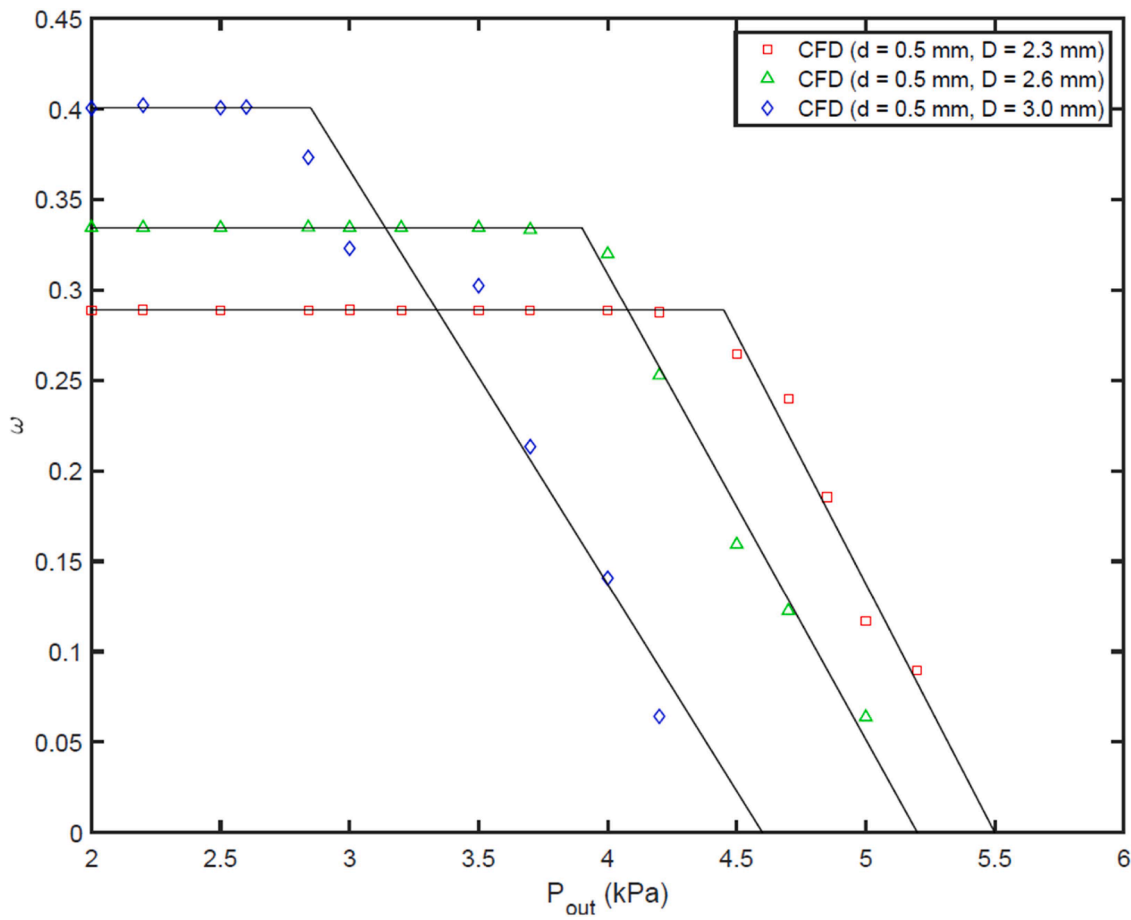


Fig. 19. Effect of D on ejector performance.

attributed to geometric asymmetries upstream of the throat in the CFD simulations or local meshing asymmetries, combined with the sensitivity of separated flow to small differences in the flow configurations on each side of the duct center plane. The DES SST $k-\omega$ model demonstrated higher accuracy in simulating the ejector performance, specifically in capturing the mixing occurring in the free shear layer, when compared to the SST $k-\omega$ model. This enhanced simulation of separated flow using the DES approach aligns with the results reported in previous studies [54–56,67].

Fig. 14 illustrates the Ma variation along the center-plane of the original VGRE using the two TMs at $P_{primary}$ of 200 kPa, $P_{secondary}$ of 1.8 kPa, and P_{out} of 2.84 kPa. The simulation results displayed that the SST $k-\omega$ TM overestimated the experimental results for the maximum ω , while the DES SST $k-\omega$ TM provided a more reasonable estimation. In terms of the shock expansion structures, the DES SST $k-\omega$ model exhibited longer downstream extensions compared to the SST $k-\omega$ model. Moreover, a higher Ma was observed around the ejector throat for the DES SST $k-\omega$ model compared to the SST $k-\omega$ model. As a result, the DES SST $k-\omega$ model drew less secondary flow into the mixing regime, leading to a reduction in the ω that was more consistent with the experimental data compared to the SST $k-\omega$ model. However, both TMs overestimated the experimental results for the r_c^* .

The variations in the P_{static} along the center-plane of the original VGRE are evident in Fig. 15, highlighting the distinct shock and expansion structures produced by the SST $k-\omega$ and DES SST $k-\omega$ TMs. Particularly, the DES SST $k-\omega$ TM generates longer shock and expansion structures along the center-plane of the ejector as indicated by distance (b) in Fig. 15 compared to the SST $k-\omega$ model as indicated by distance (a)

in Fig. 15. Both TMs exhibit a series of shock waves in the mixing regime, observed when the ejector operates under choked conditions with $P_{primary}$ of 200 kPa, $P_{secondary}$ of 1.8 kPa, and P_{out} of 2.84 kPa, respectively. It is worth noting that axial ejectors commonly exhibit two series of shock waves [68–71]: one at the exit of the primary nozzle and the other in the constant throat area of the ejector. However, in the radial ejector geometry, there is no constant throat area, which may explain the absence of a second series of shocks.

The DES SST $k-\omega$ TM exhibited superior consistent with experimental data for the ω , while the SST $k-\omega$ model showed a tendency to overestimate the results. These discrepancies can be attributed to the lower intensity of waves observed in the SST $k-\omega$ model compared to the DES SST $k-\omega$ model. As a result, the DES SST $k-\omega$ TM was selected for subsequent simulations.

6.2. Nozzle throat separation (d) effect

Fig. 16 demonstrates the impact of d values ($d = 0.4, 0.5,$ and 0.6 mm) on the effectiveness of the ejector, with a fixed ejector D of 2.3 mm. The $P_{primary}$ was set at 200 kPa, and the $P_{secondary}$ was 1.8 kPa. Decreasing the d from 0.6 mm to 0.4 mm resulted in a 62 % increase in ω , while P_{out}^* decreased by 24 %. The original VGRE exhibited higher ω values with reduced d , but this yielded lower P_{out}^* values. The nozzle and ejector area ratios increased as the d decreased.

The changes in the ω and P_{out}^* correspond approximately to the relative change in the nozzle and ejector throat areas. The ω is influenced by the available flow area (AFA), while the P_{out}^* is influenced by the relative momentum flux. When the d increases, there is a

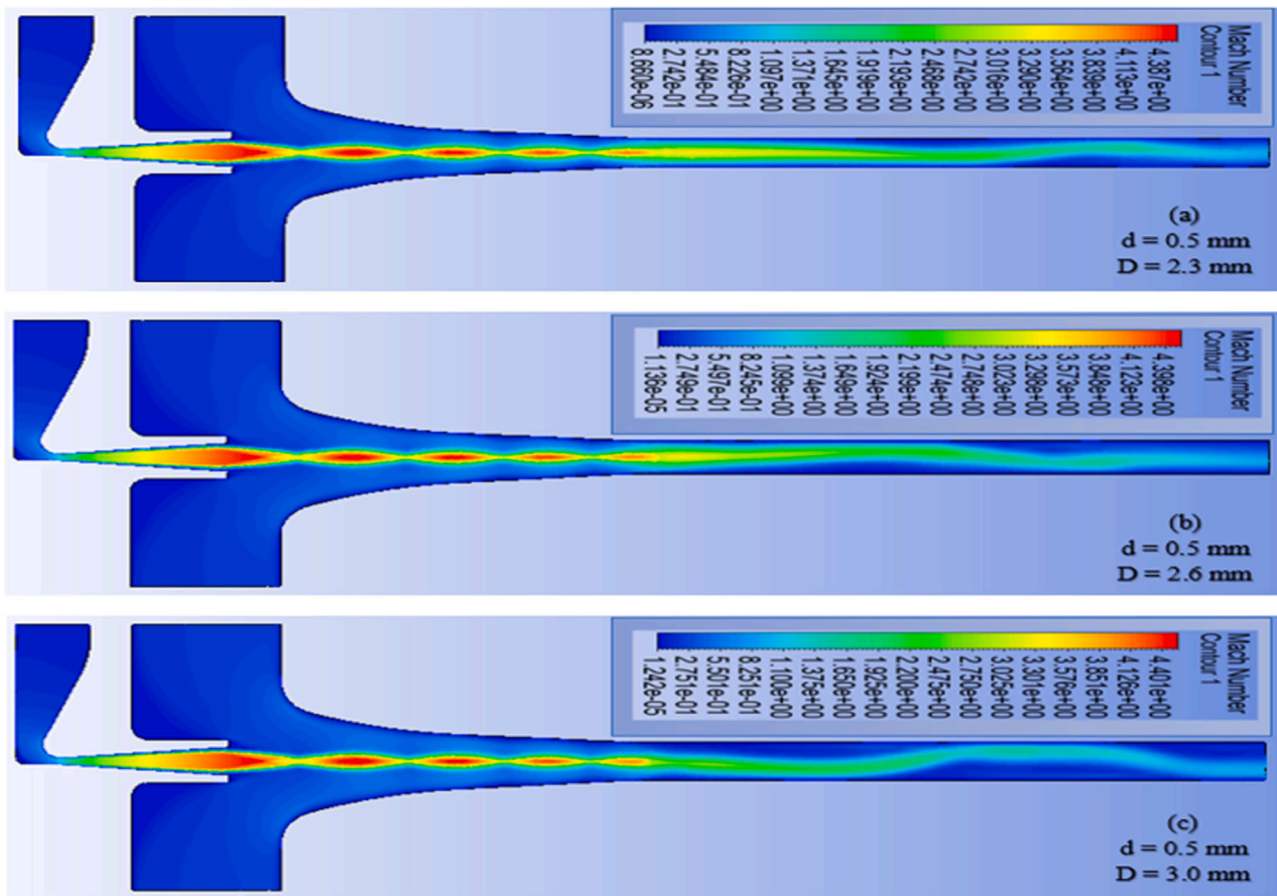


Fig. 20. Contours of Ma for different D values at an P_{out} of 2.84 kPa.

corresponding increase in the momentum flux of the primary stream relative to the secondary stream. This reduces the AFA for the secondary stream when the ejector D is held constant. As a result, increasing the d results in a higher P_{out}^* but a lower ω .

Fig. 17 illustrates the Ma contours for three different d values. The simulations were conducted at a $P_{primary}$ of 200 kPa, $P_{secondary}$ of 1.8 kPa, and P_{out} of 2.84 kPa. According to the CFD simulations, a smaller d of 0.4 mm yielded a higher ω but a lower P_{out}^* . It is important to note that the ejector operated in the choked condition for all three d values. The $\dot{m}_{primary}$ at a $P_{primary}$ of 200 kPa were 3.81, 4.76, and 5.67 g/s for d of 0.4, 0.5, and 0.6 mm, respectively. The AFA of the primary nozzle increased by 50 % when the d increased from 0.4 to 0.6 mm, resulting in a corresponding rise in the $\dot{m}_{primary}$ of about 49 %.

Fig. 18 depicts the Ma contours for different d values. The simulations were conducted at a $P_{primary}$ of 200 kPa, $P_{secondary}$ of 1.8 kPa, and P_{out} of 4.5 kPa. Similar trends in the $\dot{m}_{primary}$ were observed compared to the previous d analysis. The ejector operated in the unchoked condition for d of 0.4 and 0.5 mm, while it operated in the choked condition for a d of 0.6 mm. A noticeable increase in asymmetric flow patterns was observed when the d decreased from 0.6 to 0.4 mm, particularly at a P_{out} of 4.5 kPa. This suggests that the ejector is operating closer to the malfunction condition. The size of the primary jet core is directly proportional to the d , resulting in a decrease in the effective entrainment area available for the secondary stream. The maximum Ma decreased from approximately 4.44 to 4.30 when the d increased from 0.4 to 0.6 mm. By comparing the Ma contours for P_{out} of 2.84 kPa (Fig. 18) and 4.5 kPa (Fig. 17), it is evident that an increase in the P_{out} causes a shift of the shock structures upstream. This phenomenon has been observed and reported in other studies [26,68,72].

6.3. Duct throat separation (D) effect

The impact of D on ejector performance at a $P_{primary}$ of 200 kPa and a $P_{secondary}$ of 1.8 kPa is depicted in Fig. 19. The $\dot{m}_{primary}$ value was kept constant at 4.76 g/s for all D values, with the d fixed at 0.5 mm. Increasing the D results in an increase in the ejector area ratio. This, in turn, leads to an increase in the AFA for the secondary flow. However, the $\dot{m}_{primary}$ value remains constant as the nozzle remains choked. As a result, the ω increases by 39 % when the D is increased from 2.3 mm to 3.0 mm, while the P_{out}^* decreases by 36 %. Therefore, by altering the D , changes can be performed to the secondary flow rate in both on and off designs operations. It should be noted that increasing the D allows for higher ω in the original VGRE, but it leads to a lower P_{out}^* .

The Ma contours for three different D values are shown in Fig. 20. These simulations were performed at a $P_{primary}$ of 200 kPa, $P_{secondary}$ of 1.8 kPa, and P_{out} of 2.84 kPa. The results indicate that a larger D of 3.0 mm resulted in a higher ω but a lower P_{out}^* . The ejector operated in a choked condition for all three D values. While the $\dot{m}_{primary}$ value was kept constant at 4.76 g/s for a d of 0.5 mm, the $\dot{m}_{secondary}$ increased from 1.38 to 1.91 g/s as the D increased from 2.3 to 3.0 mm. The AFA for the secondary stream increased by approximately 30 % when the D was increased from 2.3 to 3.0 mm, resulting in a corresponding increase in the $\dot{m}_{secondary}$ of about 38 %.

The Ma contours for three different D values are depicted in Fig. 21. These simulations were conducted at a $P_{primary}$ of 200 kPa, $P_{secondary}$ of 1.8 kPa, and P_{out} of 4.0 kPa. The ejector operated in a choked condition for the 2.3 mm D , while it operated in an unchoked condition for the 2.6 and 3.0 mm D . In the case of the 3.0 mm D , the ejector operated with a

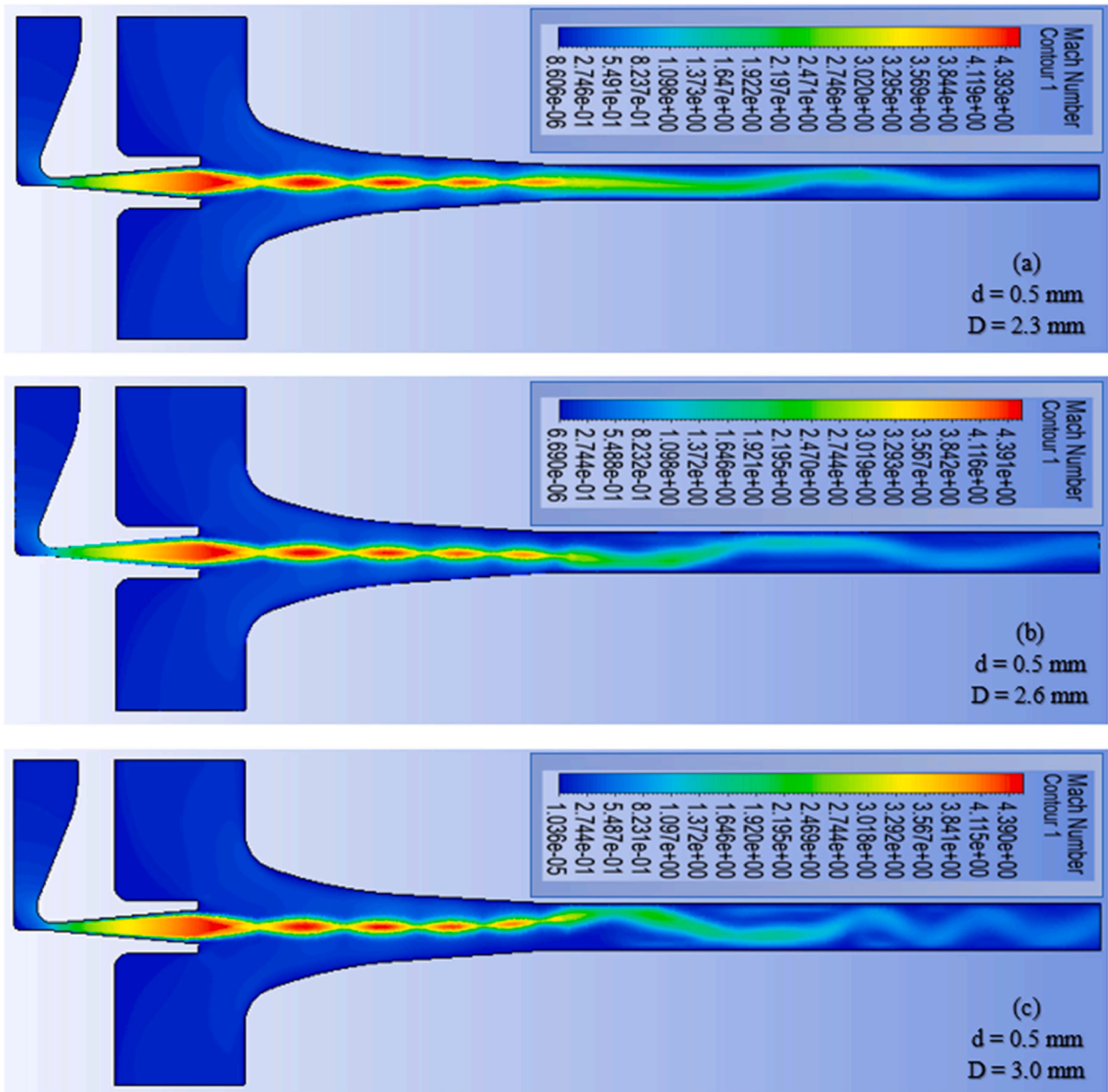


Fig. 21. Contours of Ma for different D values at an P_{out} of 4.0 kPa.

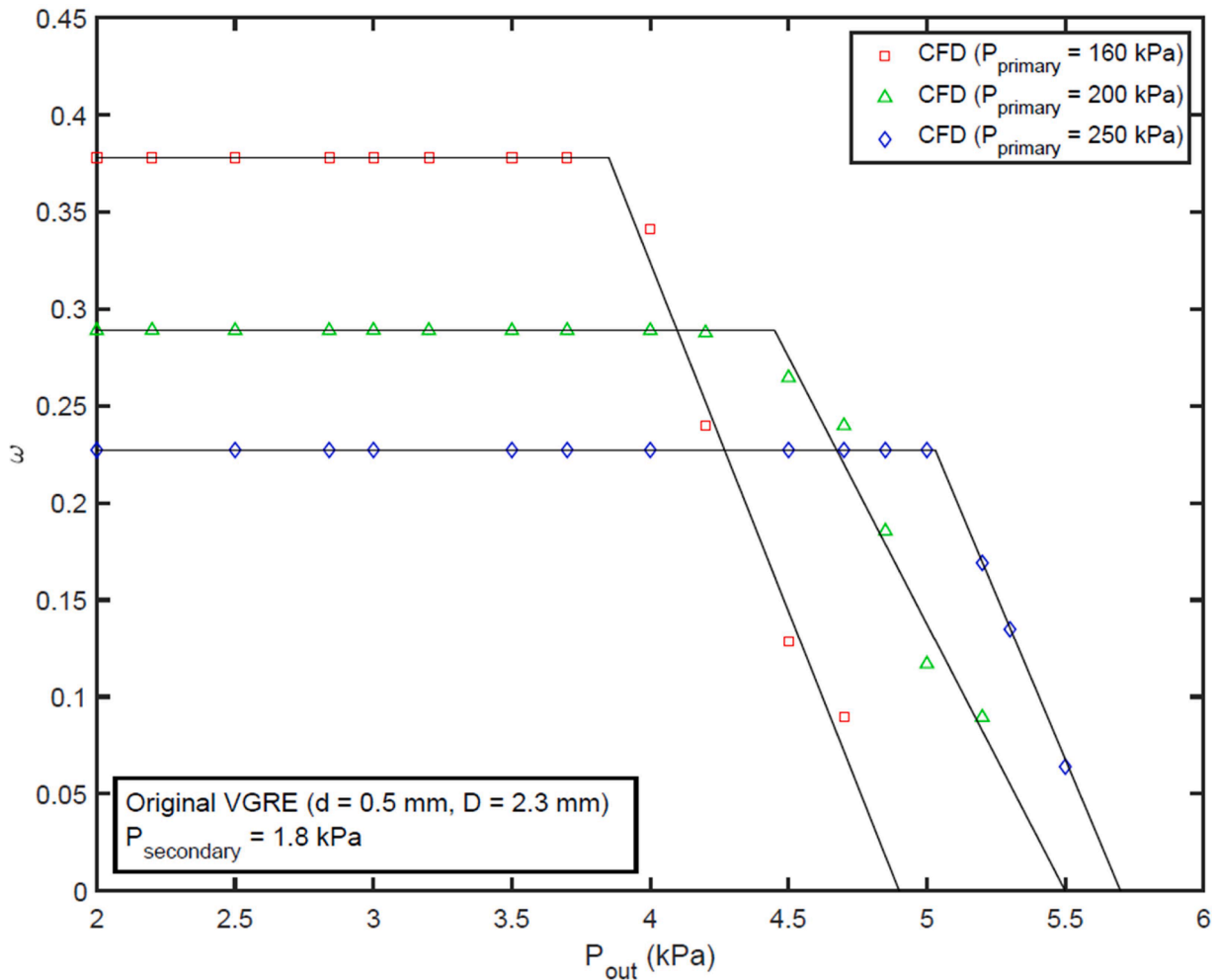


Fig. 22. Variation of ω with P_{out} at different $P_{primary}$ values.

low P_{out}^* of 2.85 kPa. The maximum Ma remained consistent at approximately 4.39 for all three D values. Comparing the Ma contours for P_{out} of 2.84 kPa as displayed in Fig. 20 and 4.0kPa as depicted in Fig. 21, similar observations can be made regarding the P_{out} , asymmetric flow, and the position of the shock structures, as discussed in Section 6.2.

6.4. Primary and secondary pressure ($P_{primary}$ and $P_{secondary}$) effects

The impact of varying primary and secondary flow pressures while maintaining fixed d and D has been examined and is depicted in Fig. 22 and Fig. 23, respectively. Fig. 22 specifically focuses on the effect of different $P_{primary}$ values with a fixed $P_{secondary}$ of 1.8 kPa and an P_{out} of 2.84 kPa. The simulations were conducted using fixed d and D of 0.5 and 2.3 mm, respectively. The CFD results revealed that as the $P_{primary}$ decreases, the ω increases, while the P_{out}^* decreases. For instance, the ω increased by approximately 66 % when $P_{primary}$ decreased from 250 to 160 kPa, resulting in a decrease in P_{out}^* by approximately 23 %. This observed behavior can be attributed to the primary jet leaving the nozzle exit becoming under-expanded when the $P_{primary}$ increases. As a result, the effective area available for entraining the secondary stream decreases. Consequently, the \dot{m} of the secondary stream decreases, while the $\dot{m}_{primary}$ increases due to the higher $P_{primary}$. As a result, the ω decreases. However, the momentum of the mixed stream increases as the $\dot{m}_{primary}$ increases, in an elevation of the in the P_{out}^* . This finding

validates the notion that higher $P_{primary}$ result in lower ω and higher P_{out}^* .

The impact of different $P_{secondary}$ values, while maintaining a fixed $P_{primary}$ of 200 kPa and P_{out} of 2.84 kPa, has been investigated and is presented in Fig. 23. The CFD simulations considered three $P_{secondary}$: 1.8, 2.5, and 3.2 kPa. The results demonstrated that the ejector performance, as indicated by the ω and the P_{out}^* , increased as the $P_{secondary}$ increased. Specifically, the ω exhibited a 54 % increase when the $P_{secondary}$ increased from 1.8 to 2.5 kPa. Similarly, the ω showed a significant increase of approximately 113 % when the $P_{secondary}$ increased from 1.8 to 3.2 kPa. In contrast, the P_{out}^* displayed a more modest increase of around 10 % and 21 % for the respective $P_{secondary}$ increments. The observed behavior can be attributed to the increase in the effective area available for the entrainment of the secondary stream as the $P_{secondary}$ rises. This results in an increased $\dot{m}_{secondary}$, which possesses a higher momentum flux. Conversely, the $\dot{m}_{primary}$ remains relatively constant. Consequently, higher ω and P_{out}^* are achieved in each case. These findings affirm that higher $P_{secondary}$ consistently lead to increased ω and P_{out}^* .

6.5. Variation of entrainment ratio (ω) with expansion ratio (r_e)

The relationship between the ω and the expansion ratio (r_e) has been investigated for various d and D , as well as different $P_{primary}$ ranging from 160 to 270 kPa, with a constant $P_{secondary}$ of 1.8 kPa. The results are presented in Figs. 24 and 25. Polynomial curves of second-order best-fit

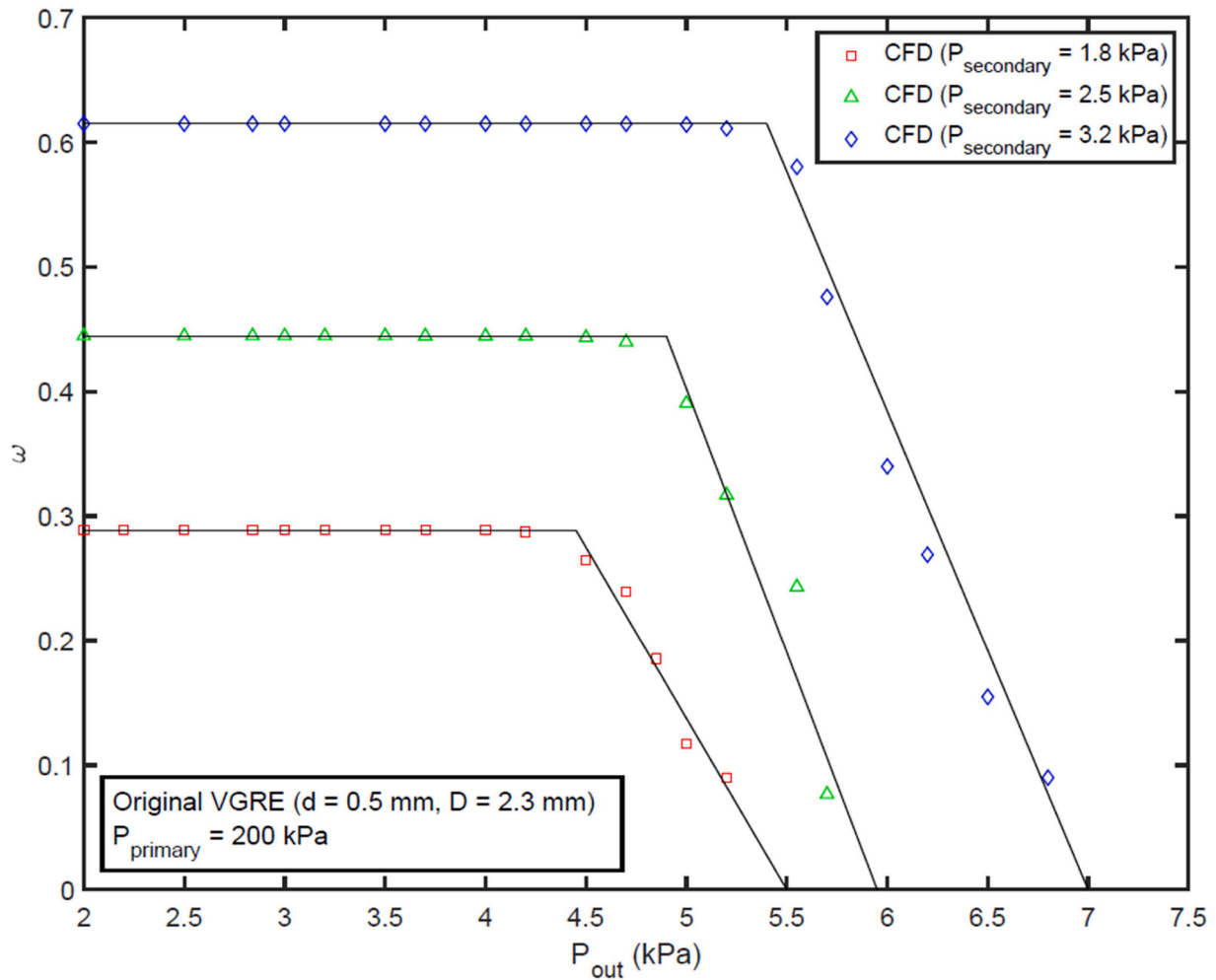


Fig. 23. Variation of ω with P_{out} at different $P_{secondary}$ values.

were generated to represent the simulation data in both figures. Fig. 24 illustrates the ω as a function of the r_e for three different d values: 0.4, 0.5, and 0.6 mm, at various operating conditions. Based on the CFD simulations, it was observed that smaller d generally result in higher ω for different r_e . This trend aligns with findings reported for axial ejectors in other studies [30,73,74]. Specifically, at a low expansion ratio of 89, the ω increased by 68 % when the d decreased from 0.6 to 0.4 mm. Furthermore, for a d of 0.4 mm, the ω increased by 90 % when the r_e decreased from 150 to 89. It is worth noting that decreasing the d leads to an increase in the ejector area ratio. Consequently, optimizing the entrainment performance requires reducing the d as the r_e increases. In summary, achieving a higher ω can be accomplished by reducing the r_e and decreasing the d . The value of r_e can be modified by either increasing the $P_{secondary}$ or decreasing the $P_{primary}$. It is important to recognize that r_e varies with changes in the operating conditions.

Fig. 25 depicts the relationship between the ω and the r_e for three different D values (2.3, 2.6, and 3.0 mm) under various operating conditions. The CFD simulations indicate that larger D result in higher ω values compared to smaller throat separations for different r_e values. Furthermore, as the r_e decreases, the expected ω increases. For instance, at a low r_e value of 89, increasing the D from 2.3 to 3.0 mm leads to a 29 % increase in ω . Similarly, when the r_e decreases from 150 to 89 for a D of 2.3 mm, the ω value rises by 86 %. These results align with the trend observed in the ejector area ratio, which increases with increasing D . This increase in available flow area for the secondary flow contributes to

higher entrainment ratios. Consequently, adjusting the D can optimize the entrainment performance, achieving higher ω values by decreasing the r_e and increasing the D .

6.6. Variation of critical compression ratio (r_c^*) with expansion ratio (r_e)

The relationship between the r_c^* and the r_e has been explored for different d and D , as depicted in Fig. 26 and Fig. 27. The r_e values and the approximating functions used in the simulations are consistent with those detailed in Section 6.5. Fig. 26 illustrates the r_c^* as a function of r_e for three d values of 0.4, 0.5, and 0.6 mm under various operating conditions. Based on the CFD simulations, larger d yield higher r_c^* values compared to smaller throat separations for different r_e values. Furthermore, increasing the r_e leads to an increase in the expected r_c^* . This finding aligns with previous studies conducted by several researchers [68,75–78]. For instance, at a low r_e value of 89, increasing the d from 0.4 mm to 0.6 mm results in a 34 % increase in r_c^* . Similarly, when the r_e value increases from 89 to 150 for a d of 0.4 mm, the r_c^* value increases by 19 %. The increase in r_c^* is attributed to the increase in momentum flux of the primary stream relative to that of the secondary stream when the d decreases. Consequently, to optimize the r_c^* , the d should be increased when the r_e decreases. In summary, higher r_c^* values can be achieved by increasing the r_e and increasing the d [68,75–78].

Fig. 27 illustrates the relationship between the r_c^* and the r_e for three different duct throat separations (2.3, 2.6, and 3.0 mm) under various

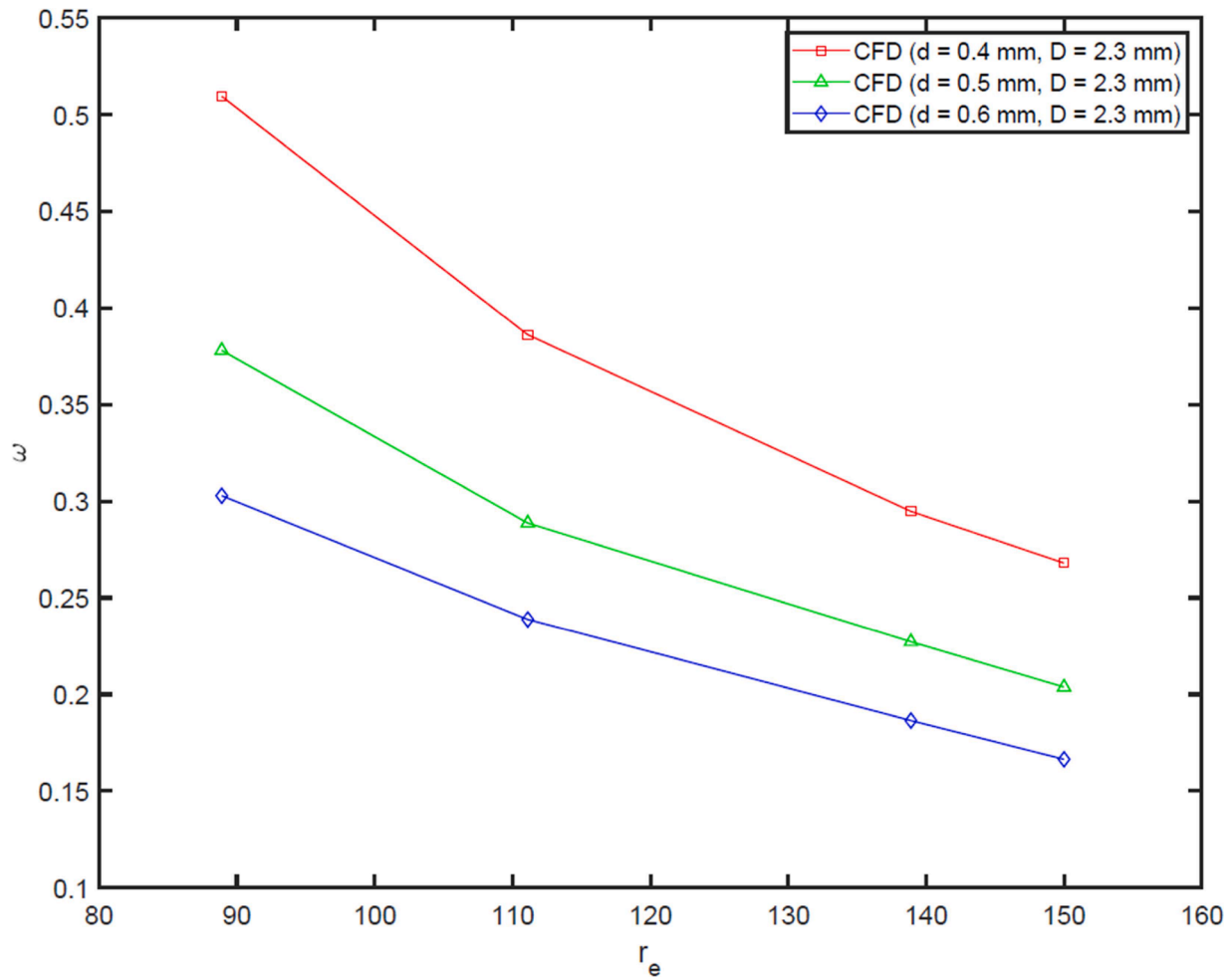


Fig. 24. Variation of ω with r_e at different d values.

operating conditions. The CFD simulations indicate that smaller D result in higher r_c^* values compared to larger separations for different r_e values. For instance, at a low r_e value of 89, reducing the D from 3.0 to 2.3 mm led to a 52 % increase in r_c^* . Similarly, when the r_e value increased from 89 to 150 for a D of 2.3 mm, the r_c^* value increased by 26 %. This observation can be attributed to the increased momentum flux of the primary stream relative to the secondary stream when the D decreases. Consequently, decreasing the D is recommended to enhance the r_c^* for a given set of operating conditions and geometry parameters, particularly when the r_e value decreases. In summary, achieving a higher r_c^* can be accomplished by increasing the r_e value and decreasing the D value.

6.7. Executive summary for CFD results

The impact of both d and D on the performance of the original VGRE was investigated across a range of working conditions. The study involved numerical evaluations of the original VGRE at P_{primary} of 160, 200, 250, and 270 kPa, as well as $P_{\text{secondary}}$ of 1.8, 2.5, and 3.2 kPa, with P_{out} approximately ranging from 2 kPa to 7 kPa. Based on the CFD results, the original VGRE exhibited ω values ranging from 0.16 to 0.61, P_{out}^* values between 2.64 and 5.53 kPa, r_c^* values between 1.5 and 3.1, and η values between 7 % and 17 % at r_e values ranging from 89 to 150 for different d and D . The ejector area ratio increased with decreasing d or increasing D . To achieve higher ω values, it was found beneficial to decrease the r_e , decrease the d , and increase the D . Conversely, to attain higher r_c^* values, it was advantageous to increase the r_e value, increase

the d , and decrease the D . However, increasing the r_e value, increasing the d , and decreasing the D resulted in higher r_c^* . Table 5 provides a summary of the key simulated results for the different operating conditions and ejector parameters of the original VGRE.

Based on the available information from Rahimi's [15] experiments, the simulations conducted in this study demonstrated that both the DES SST $k-\omega$ and SST $k-\omega$ TMs exhibited similar levels of consistency with the experimental data for the wall P_{static} in both on-design and off-design operations. The average errors in the simulated P_{static} , compared to the experimental data, were approximately 10 % for both models in both operating conditions. However, neither CFD-TM achieved a high level of consistency with Rahimi's experimental data for the wall P_{static} in both the on-design and off-design operations. Furthermore, the DES SST $k-\omega$ TM demonstrated more consistent results with the experimental data for both choked and unchoked conditions in the mixing section, in comparison to the SST $k-\omega$ TM. In contrast, both TMs exhibited less consistency with the experimental data for both choked and unchoked conditions in the diffuser section. This research provides a foundation for future explorations and advancements in the field of adjustable supersonic radial ejectors using DES models.

Although the 2-D simulations conducted in this study have certain limitations in accurately predicting the performance of the radial ejector compared to the experimental results, the 2-D simulation captures the general characteristics of the experiment. Furthermore, the 2-D simulations exhibit similar trends to the experimental data, particularly when examining variations in the operating conditions. This indicates the

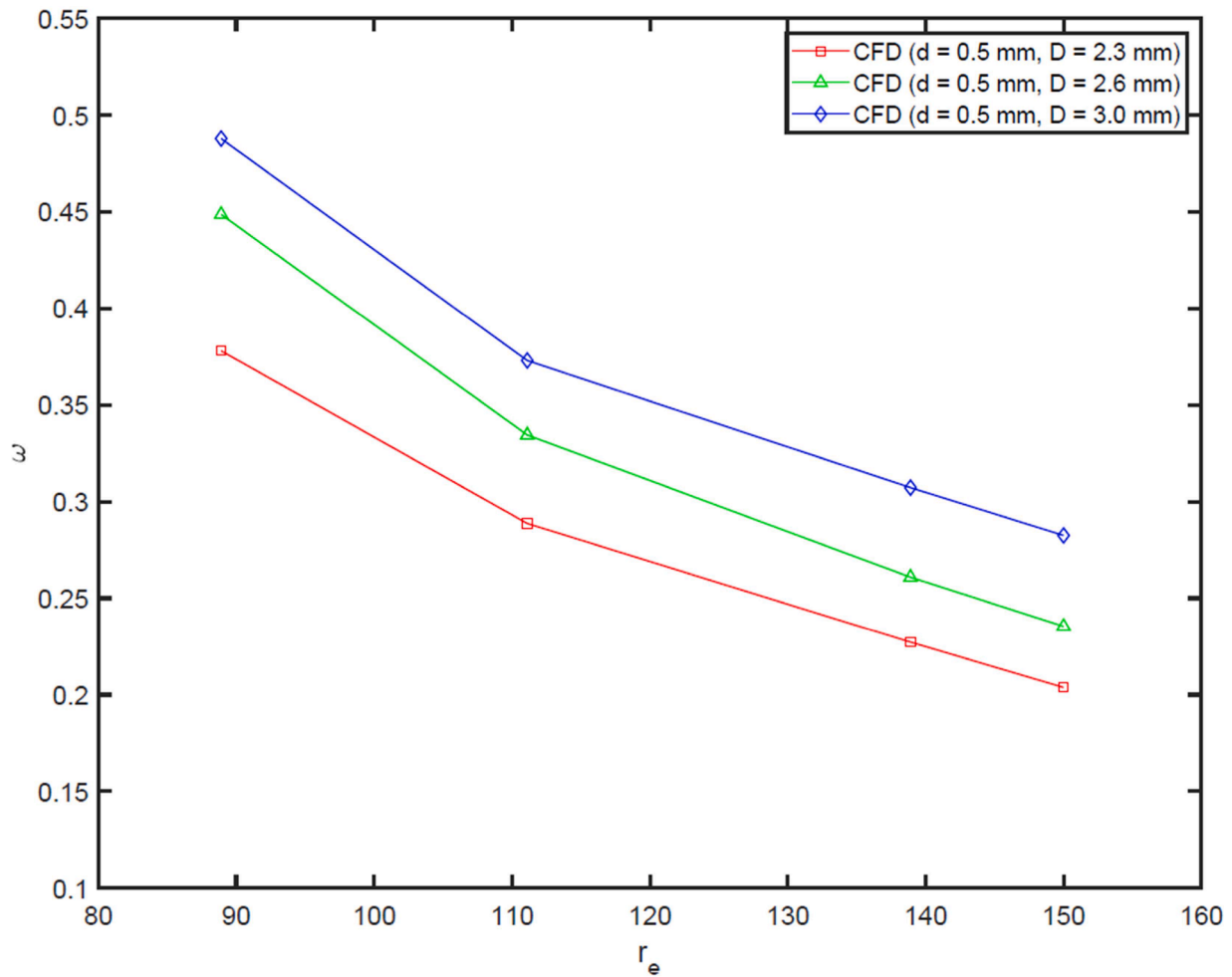


Fig. 25. Variation of ω with r_e at different D values.

validity and usefulness of the 2-D simulations, especially when employing the most accurate TMs identified for simulating the original VGRE under on-design conditions. However, it should be noted that DES-TMs are typically better suited for 3-D simulations, as they can effectively capture the largest unsteady vortices present in turbulent flows, as suggested by some researchers [56,79]. Beyond the critical mode or off-design conditions, 3-D simulations may provide more precise and accurate results compared to the 2-D simulations.

6.8. Prediction and optimization results

The experiments were conducted on a computer system operating Windows 11 64-bit, equipped with an 11th-generation Intel Core i5-1135G7 processor and 8 GB of RAM. Python 3.7 and Matlab R2022a software were used. The experiment consisted of two primary phases. First, a multi-output GPR model was utilized to predict the relationship between various factors and their corresponding responses. Second, a multi-objective MPA optimization approach was employed to maximize three objectives: (i) entrainment ratio, (ii) critical compression ratio, and (iii) ejector efficiency.

6.8.1. Prediction results and model evaluation

The experimental dataset employed to construct the multi-output GPR model aimed to establish relationships among the following variables: BCs (P_{primary} and $P_{\text{secondary}}$), Geometry (d and D), and the resulting outcomes, encompassing entrainment ratio, critical compression ratio,

and ejector efficiency.

A 5-fold cross-validation technique is employed to assess prediction performance and mitigate overfitting. In this process, the dataset is randomly divided into five equally-sized subsets. During each iteration, one of these subsets is designated as the validation data, while the remaining four are used for training. The model is then trained on the training data and evaluated using the validation data. This process is repeated five times, with each subset serving as the validation data once. Finally, the cross-validated result is determined by averaging the outcomes from these five rounds. This approach ensures a comprehensive evaluation of the model's performance across diverse data subsets, reducing the risk of overfitting and providing a robust assessment of its predictive capabilities.

The strength of the relationship between the multi-output GPR model and the dependent variables is quantified using the coefficient of determination (R^2), while the accuracy of predictions is evaluated through the root mean square error (RMSE), as presented in Table 6. These two metrics are computed to gauge the effectiveness and performance of the multi-output GPR model. Based on the data presented in 6, the multi-output GPR model demonstrates strong predictive performance across the evaluated response variables, which include entrainment ratio, critical compression ratio, and ejector efficiency. This is evidenced by low RMSE values, signifying a high degree of accuracy in predictions. Additionally, the R^2 values are notably high, indicating a robust relationship between the model's predictions and the actual values.

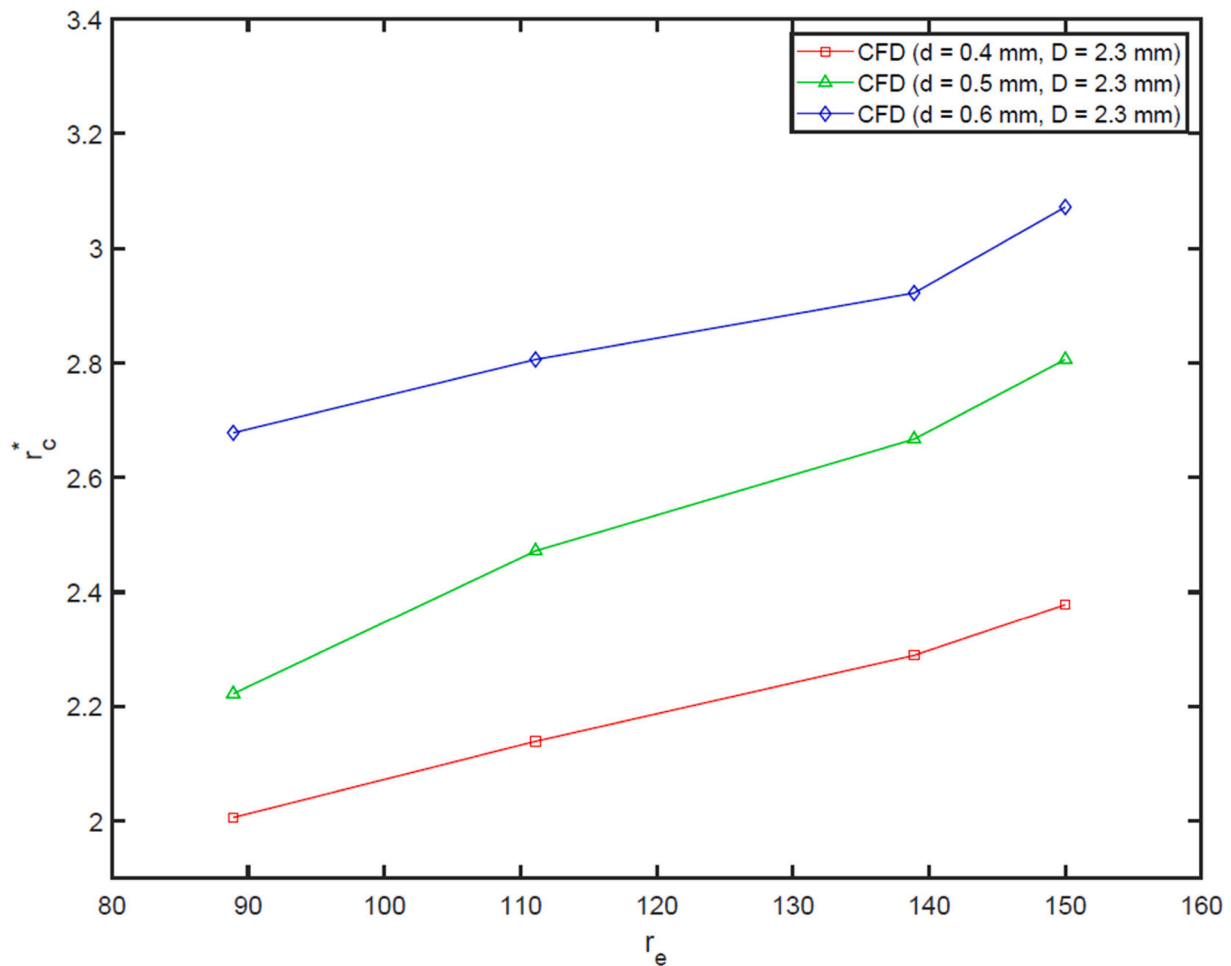


Fig. 26. Variation of r_c^* with r_e at different d values.

Graphic representation plays a vital role when assessing the GPR model. In this context, the accuracy of predictive models was visually demonstrated by plotting their predictions against the corresponding targets, as depicted in Fig. 28. This graphical representation highlights the capability of the GPR model to replicate the provided observations accurately. It is evident that the predictions closely align with the actual targets, forming a tight cluster along the diagonal line. This alignment signifies the high R^2 values observed in the previous analysis, further underscoring the robustness of the GPR model's predictions.

6.8.2. Optimization results

The Multi-objective MPA approach is employed to optimize the output of the multi-output GPR model by identifying the optimal input parameter values. The primary objective of this optimization process is to identify the most favorable values for each set of boundary conditions (P_{primary} and $P_{\text{secondary}}$) and geometric parameters (d and D) in order to maximize the entrainment ratio (ω), critical compression ratio (r_c^*), and ejector efficiency (η).

Table 7 presents the optimal values for the BCs (P_{primary} and $P_{\text{secondary}}$) and geometric parameters (d and D) that yield the maximum values for ω , r_c^* , and η . The highest values achieved were $\omega = 0.303$, $r_c^* = 2.678$, and $\eta = 0.156$, corresponding to the following parameter settings: $P_{\text{primary}} = 160$ kPa, $P_{\text{secondary}} = 1.8$ kPa, $d = 0.6$ mm, and $D = 2.3$ mm, respectively.

7. Conclusion

Numerical simulations were performed using ANSYS FLUENT - CFD models to investigate the original VGRE. Both RANS and DES methods were employed to simulate turbulence. The CFD analysis of the VGRE, which operated with air, was conducted using a 2-dimensional axisymmetric model. Furthermore, this study has successfully integrated two crucial stages in the pursuit of optimizing eject performance systems. First, the utilization of a multi-output GPR model facilitated precise predictions by establishing intricate relationships between boundary conditions (P_{primary} and $P_{\text{secondary}}$), geometric parameters (d and D), and response variables (entrainment ratio, critical compression ratio, and ejector efficiency). Second, the implementation of the Marine Predators Algorithm (MPA) as a multi-objective optimization approach enabled the identification of optimal input parameters. The following conclusions were drawn from the study:

- Among the RANS and DES models considered; the DES SST k- ω TM demonstrated significant consistency with the experimental data for the original VGRE. The average discrepancy between the simulated ω and the experimental data was only 5 % for the DES SST k- ω model.
- The SST k- ω and DES SST k- ω TM showed a tendency to overestimate the experimental results for the r_c^* . The discrepancy between the experiments and the simulated ω could be attributed to differences in the secondary flow rate. The DES SST k- ω TM poorly simulated the r_c^* .

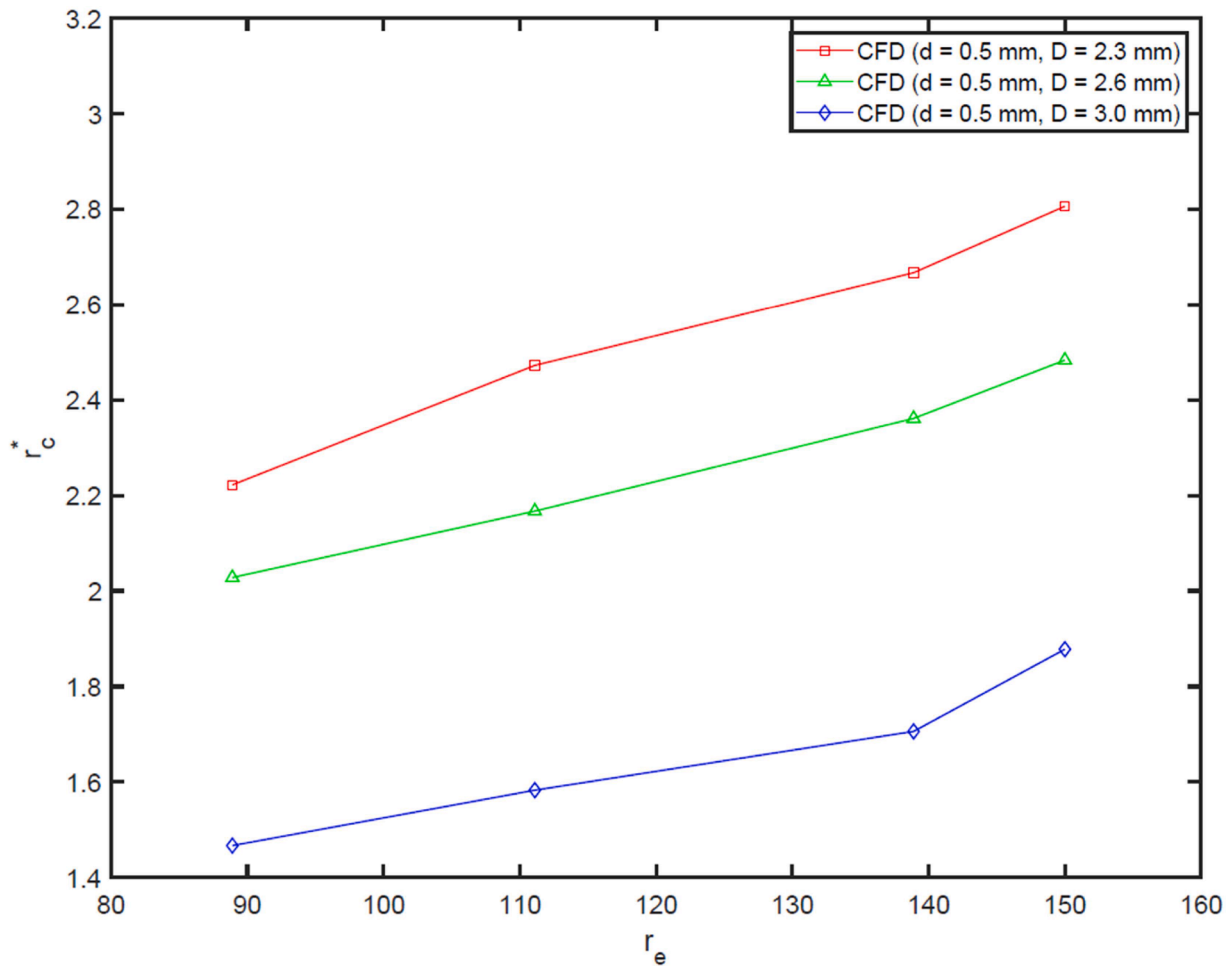


Fig. 27. Variation of r_c^* with r_e at different D values.

Table 5

Main simulated outcomes for the tested operating conditions and the ejector parameters for the original VGRE.

Parameter	Outcomes
$P_{primary} \uparrow$	$\omega \downarrow, P_{out}^* \uparrow, r_c^* \uparrow$
$P_{secondary} \uparrow$	$\omega \uparrow, P_{out}^* \uparrow, r_c^* \uparrow$
$r_e \uparrow$	$P_{primary} \uparrow, P_{secondary} \downarrow$
$r_e \uparrow$	$\omega \downarrow, P_{out}^* \uparrow, r_c^* \uparrow$
$d \uparrow$	$\omega \downarrow, P_{out}^* \uparrow, r_c^* \uparrow$
$D \uparrow$	$\omega \uparrow, P_{out}^* \downarrow, r_c^* \downarrow$

Table 6

Statistical evaluation of the multi-output GPR model.

Response	RMSE	R ²
Entrainment ratio (ω)	0.0077	0.9948
Critical compression ratio	0.043	0.989
Ejector efficiency	0.051	0.9812

- The proposed numerical approach using DES models still faced challenges in accurately modeling the boundary of the off-design model, which may be related to the design of the mixing section.
- Off-design conditions introduced additional complexity, as the entrainment of the secondary stream became more reliant on the accuracy of the mixing simulations. This added complexity can also be attributed to the occurrence of shock processes, which resulted in

a highly intricate flow in the unchoked state and unexpected experimental outcomes in terms of r_c^* values.

- Discrepancies between experimental and simulation results for wall P_{static} and high r_c^* could potentially be attributed to geometric factors and unsteady flow phenomena.
- This research opens up opportunities for further experimental investigations of VGREs, with a focus on enhancing the performance of the original VGRE using DES models. Therefore, additional CFD investigations utilizing DES models are necessary to validate future experimental studies for VGREs and compare the findings with previous works.
- Based on the CFD results, the original VGRE exhibited ω values ranging from 0.16 to 0.61, r_c^* values between 1.5 and 3.1, and η values between 7 % and 17 % at expansion ratio (r_e) values ranging from 89 to 150 for different nozzle throat separations (d) and different duct throat separations (D).
- The multi-output GPR model demonstrates its reliability and effectiveness in predicting these response variables within the experimental framework, consistently offering accurate estimates with a strong correlation to the observed data. This is substantiated by the presence of low RMSE values, all below 0.051, and high R² values, all exceeding 0.9812.
- The optimal parameter values that maximize the entrainment ratio (ω), critical compression ratio (r_c^*), and ejector efficiency (η), are as follows: $P_{primary} = 160$ kPa, $P_{secondary} = 1.8$ kPa, $d = 0.6$ mm, and $D = 2.3$ mm. These specific parameter combinations resulted in achieving

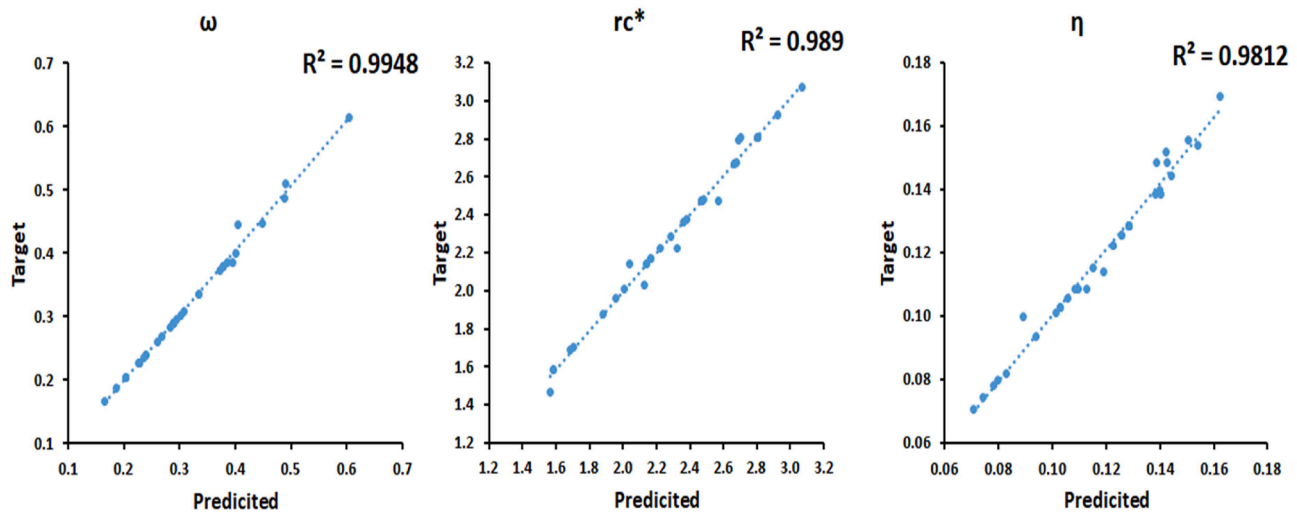


Fig. 28. Multi-output GPR model prediction precision.

Table 7

Optimized results utilizing the GPR model and Multi-objective MPA approach.

Factors				Objectives		
P_{primary} (kPa)	$P_{\text{secondary}}$ (kPa)	d (mm)	D (mm)	ω (-)	r_c^* (-)	η (-)
160	1.8	0.6	2.3	0.303	2.678	0.156

the highest values for each respective objective: $\omega = 0.303$, $r_c^* = 2.678$, and $\eta = 0.156$.

- The integration of GPR-ML and the MPA offers a powerful solution for complex optimization and predictive tasks. This robust combines GPR's data-driven modeling with MPA's dynamic optimization, enabling accurate modeling of relationships and efficient parameter optimization. This approach holds significant promise across diverse fields, enhancing problem-solving and decision-making with the combined strengths of ML and nature-inspired algorithms.

Declaration of Competing Interest

The authors declare that they have no known competing financial interests or personal relationships that could have appeared to influence the work reported in this paper.

Data availability

Data will be made available on request.

References

- [1] M. Tavakoli, M. Nili-Ahmadabadi, A. Joulaei, M.Y. Ha, Enhancing subsonic ejector performance by incorporating a fluidic oscillator as the primary nozzle: a numerical investigation, *Int. J. Thermofluids*. 20 (2023), 100429.
- [2] A. Alahmer, S. Ajib, Solar cooling technologies: state of art and perspectives, *Energy Convers. Manag.* 214 (2020), 112896.
- [3] S. Li, Q. Liu, J. Lu, X. Li, F. Lu, L. Xie, J. Chen, L. Yang, Y. Zeng, Comparative study on two low-grade heat driven ejection-compression refrigeration cycles with evaporator-condenser and evaporator-subcooler, *Therm. Sci. Eng. Prog.* 45 (2023), 102080.
- [4] R. Al-Rbaihat, R. Malpress, D. Buttsworth, K. Saleh, Detached eddy simulation of an adjustable radial ejector, in: *Proc. 21st Australas. Fluid Mech. Conf., Australasian Fluid Mechanics Society*, 2018.
- [5] A.S. Chowdhury, M.M. Ehsan, A critical overview of working fluids in organic rankine, supercritical rankine, and supercritical brayton cycles under various heat grade sources, *Int. J. Thermofluids*. (2023), 100426.
- [6] S. Ajib, A. Alahmer, Solar cooling technologies, energy conversion-current technol, *Futur, Trends, IntechOpen*, London, UK, 2018. <https://doi.org/10.5772/intechopen.80484>.
- [7] S. Varga, A.C. Oliveira, A. Palmero-Marrero, J. Vrba, Preliminary experimental results with a solar driven ejector air conditioner in Portugal, *Renew. Energy*. 109 (2017) 83–92.
- [8] H.J. Mosleh, A. Hakkaki-Fard, M. DaqiqShirazi, A year-round dynamic simulation of a solar combined, ejector cooling, heating and power generation system, *Appl. Therm. Eng.* 153 (2019) 1–14.
- [9] B. Tashtoush, Y. Nayfeh, Energy and economic analysis of a variable-geometry ejector in solar cooling systems for residential buildings, *J. Energy Storage*. 27 (2020), 101061.
- [10] Y. Bartosiewicz, Z. Aidoun, P. Desevaux, Y. Mercadier, Numerical and experimental investigations on supersonic ejectors, *Int. J. Heat Fluid Flow*. 26 (2005) 56–70.
- [11] G. Besagni, N. Cristiani, Multi-scale evaluation of an R290 variable geometry ejector, *Appl. Therm. Eng.* 188 (2021), 116612.
- [12] C.A. Garris, W.J. Hong, C. Mavriplis, J. Shipman, A new thermally driven refrigeration system with environmental benefits. *Proc. 33rd Intersoc. Eng. Conf. Energy Conversion, Color. Springs, USA*, 1998.
- [13] M. Gheorghiu, P.-D. Oprea-Stănescu, Regarding the influence of geometrical parameters on the performances of a supersonic ejector, *Univ. Timisoara, 6th Int. Conf. Hydraul. Mach. Hydrodyn. Rom.* (2004).
- [14] A.K. Ababaneh, C.A. Garris, A.M. Jawarneh, H. Tilan, Investigation of the Mach number effects on fluid-to-fluid interaction in an unsteady ejector with a radial-flow diffuser, *JJMIE* 3 (2009) 131–140.
- [15] H. Rahimi, Investigation of radial flow ejector performance through experiments and computational simulations, Ph.D. Dissertation, University of Southern Queensland, 2017.
- [16] R. Al-Rbaihat, K. Saleh, R. Malpress, D. Buttsworth, Experimental investigation of a novel variable geometry radial ejector, *Appl. Therm. Eng.* 233 (2023), 121143.
- [17] Y. Wu, H. Zhao, C. Zhang, L. Wang, J. Han, Optimization analysis of structure parameters of steam ejector based on CFD and orthogonal test, *Energy* 151 (2018) 79–93.
- [18] F. Riaz, P.S. Lee, S.K. Chou, Thermal modelling and optimization of low-grade waste heat driven ejector refrigeration system incorporating a direct ejector model, *Appl. Therm. Eng.* 167 (2020), 114710.
- [19] C.-M. Udriou, A. Mota-Babiloni, P. Giménez-Prades, Á. Barragán-Cervera, J. Navarro-Esbrí, Two-stage cascade configurations based on ejectors for ultra-low temperature refrigeration with natural refrigerants, *Int. J. Thermofluids*. 17 (2023), 100287.
- [20] H. Samsam-Khayani, S.Y. Yoon, M. Kim, K.C. Kim, Experimental and Numerical Study on Low-Temperature Supersonic Ejector, *Int. J. Thermofluids*. (2023), 100407.
- [21] M. Kadivar, D. Tormey, G. McGranahan, A comparison of RANS Models used for CFD prediction of turbulent flow and heat transfer in rough and smooth channels, *Int. J. Thermofluids*. (2023), 100399.
- [22] V.J. de Oliveira Marum, L.B. Reis, F.S. Maffei, S. Ranjbarzadeh, I. Korkischko, R. dos Santos Gioria, J.R. Meneghini, Performance analysis of a water ejector using computational fluid dynamics (CFD) simulations and mathematical modeling, *Energy* 220 (2021), 119779.
- [23] A. Jafarian, M. Azizi, P. Forghani, Experimental and numerical investigation of transient phenomena in vacuum ejectors, *Energy* 102 (2016) 528–536.
- [24] P.S. Penumadu, A.G. Rao, Numerical investigations of heat transfer and pressure drop characteristics in multiple jet impingement system, *Appl. Therm. Eng.* 110 (2017) 1511–1524.
- [25] G. Besagni, F. Inzoli, Computational fluid-dynamics modeling of supersonic ejectors: screening of turbulence modeling approaches, *Appl. Therm. Eng.* 117 (2017) 122–144.

- [26] T. Sriveerakul, S. Aphornratana, K. Chunnanond, Performance prediction of steam ejector using computational fluid dynamics: part 1. Validation of the CFD results, *Int. J. Therm. Sci.* 46 (2007) 812–822.
- [27] P. Zheng, B. Li, J. Qin, CFD simulation of two-phase ejector performance influenced by different operation conditions, *Energy* 155 (2018) 1129–1145.
- [28] Z. Chen, X. Jin, A. Shimizu, E. Hihara, C. Dang, Effects of the nozzle configuration on solar-powered variable geometry ejectors, *Sol. Energy*. 150 (2017) 275–286.
- [29] L. Wang, J. Liu, T. Zou, J. Du, F. Jia, Auto-tuning ejector for refrigeration system, *Energy* 161 (2018) 536–543.
- [30] S. Mohamed, Y. Shatilla, T. Zhang, CFD-based design and simulation of hydrocarbon ejector for cooling, *Energy* 167 (2019) 346–358.
- [31] C. Li, Y. Li, L. Wang, Configuration dependence and optimization of the entrainment performance for gas–gas and gas–liquid ejectors, *Appl. Therm. Eng.* 48 (2012) 237–248.
- [32] F. Mazzelli, A.B. Little, S. Garimella, Y. Bartosiewicz, Computational and experimental analysis of supersonic air ejector: turbulence modeling and assessment of 3D effects, *Int. J. Heat Fluid Flow*. 56 (2015) 305–316.
- [33] Y. Bartosiewicz, Z. Aidoun, P. Desevaux, Y. Mercadier, CFD-experiments integration in the evaluation of six turbulence models for supersonic ejectors modeling, *Integr. CFD Exp. Conf. Glas. UK* (2003).
- [34] J. Kolář, V. Dvořák, Verification of $k-\omega$ SST turbulence model for supersonic internal flows, *Int. J. Mech. Mechatronics Eng.* 5 (2011) 1715–1719.
- [35] E. Bumrungrthaichachan, N. Ruangtrakoon, T. Thongtip, Performance investigation for CRMC and CPM ejectors applied in refrigeration under equivalent ejector geometry by CFD simulation, *Energy Reports* 8 (2022) 12598–12617.
- [36] A.S. Ramesh, S.J. Sekhar, Experimental and numerical investigations on the effect of suction chamber angle and nozzle exit position of a steam-jet ejector, *Energy* 164 (2018) 1097–1113.
- [37] G. Besagni, Ejectors on the cutting edge: the past, the present and the perspective, *Energy* 170 (2019) 998–1003.
- [38] A. Hakkaki-Fard, Z. Aidoun, M. Ouzzane, A computational methodology for ejector design and performance maximisation, *Energy Convers. Manag.* 105 (2015) 1291–1302.
- [39] A. Alahmer, R.M. Ghoniem, Improving automotive air conditioning system performance using composite nano-lubricants and fuzzy modeling optimization, *Sustainability* 15 (2023) 9481.
- [40] H. Rezk, A.G. Olabi, M.A. Abdelkareem, A. Alahmer, E.T. Sayed, Maximizing green hydrogen production from water electrocatalysis: modeling and optimization, *J. Mar. Sci. Eng.* 11 (2023) 617.
- [41] R.M. Ghoniem, T. Wilberforce, H. Rezk, S. As' ad, A. Alahmer, Boosting power density of proton exchange membrane fuel cell using artificial intelligence and optimization algorithms, *Membranes (Basel)* 13 (2023) 817.
- [42] M. Alrbai, H. Alahmer, A. Alahmer, R. Al-Rbaihat, A. Aldalou, S. Al-Dahidi, H. Hayajneh, Retrofitting conventional chilled-water system to a solar-assisted absorption cooling system: modeling, polynomial regression, and grasshopper optimization, *J. Energy Storage*. 65 (2023), 107276, <https://doi.org/10.1016/j.est.2023.107276>.
- [43] R. Al-Rbaihat, H. Alahmer, A. Alahmer, Y. Altork, A. Al-Manea, K.Y.E. Awwad, Energy and exergy analysis of a subfreezing evaporator environment ammonia-water absorption refrigeration cycle: machine learning and parametric optimization, *Int. J. Refrig.* 154 (2023) 182–204, <https://doi.org/10.1016/j.ijrefrig.2023.07.010>.
- [44] H. Alahmer, A. Alahmer, M.I. Alamyreh, M. Alrbai, R. Al-Rbaihat, A. Al-Manea, R. Alkhazaleh, Optimal water addition in emulsion diesel fuel using machine learning and sea-horse optimizer to minimize exhaust pollutants from diesel engine, *Atmosphere (Basel)* 14 (2023) 449, <https://doi.org/10.3390/atmos14030449>.
- [45] H. Alahmer, A. Alahmer, R. Alkhazaleh, M. Alrbai, Exhaust emission reduction of a SI engine using acetone–gasoline fuel blends: modeling, prediction, and whale optimization algorithm, *Energy Reports* 9 (2023) 77–86.
- [46] A. Alahmer, H. Alahmer, A. Handam, H. Rezk, Environmental assessment of a diesel engine fueled with various biodiesels blends: polynomial regression and grey wolf optimization, *Sustainability* 14 (2022) 1367.
- [47] T. Beran, J. Gärtner, T. Koch, A model-based approach for a control strategy of a charge air cooling concept in an ejector refrigeration cycle, *Automot. Engine Technol.* 6 (2021) 203–217.
- [48] T. Hai, F.A. Alenizi, A.H. Mohammed, V. Goyal, R.K. Marjan, K. Quzwain, A.S. M. Metwally, Solid oxide fuel cell energy system with absorption-ejection refrigeration optimized using a neural network with multiple objectives, *Int. J. Hydrogen Energy*. (2023). <https://doi.org/10.1016/j.ijhydene.2023.07.115>.
- [49] H. Zhu, J. Liu, J. Yu, P. Yang, Artificial neural network-based predictive model for supersonic ejector in refrigeration system, *Case Stud. Therm. Eng.* 49 (2023), 103313.
- [50] K. Abbady, N. Al-Mutawa, A. Almutairi, The performance analysis of a variable geometry ejector utilizing CFD and artificial neural network, *Energy Convers. Manag.* 291 (2023), 117318.
- [51] K.E. Ringstad, K. Banasiak, Å. Ervik, A. Hafner, Machine learning and CFD for mapping and optimization of CO₂ ejectors, *Appl. Therm. Eng.* 199 (2021), 117604.
- [52] H. Wang, W. Cai, Y. Wang, Modeling of a hybrid ejector air conditioning system using artificial neural networks, *Energy Convers. Manag.* 127 (2016) 11–24.
- [53] R.H. Al-Rbaihat, Design of variable geometry radial ejector for HVAC purposes through experiments and simulation, Ph.D. Dissertation, University of Southern Queensland, 2020.
- [54] S. Ruck, F. Arbeiter, Detached eddy simulation of turbulent flow and heat transfer in cooling channels roughened by variously shaped ribs on one wall, *Int. J. Heat Mass Transf.* 118 (2018) 388–401.
- [55] P.R. Spalart, Detached-eddy simulation, *Annu. Rev. Fluid Mech.* 41 (2009) 181–202.
- [56] L. Zhou, R. Zhao, W. Yuan, An investigation of interface conditions inherent in detached-eddy simulation methods, *Aerosp. Sci. Technol.* 74 (2018) 46–55.
- [57] Y. Han, X. Wang, H. Sun, G. Zhang, L. Guo, J. Tu, CFD simulation on the boundary layer separation in the steam ejector and its influence on the pumping performance, *Energy* 167 (2019) 469–483.
- [58] K. Ariafar, D. Buttsworth, G. Al-Doori, R. Malpress, Effect of mixing on the performance of wet steam ejectors, *Energy* 93 (2015) 2030–2041.
- [59] G. Besagni, R. Mereu, P. Chiesa, F. Inzoli, An Integrated Lumped Parameter-CFD approach for off-design ejector performance evaluation, *Energy Convers. Manag.* 105 (2015) 697–715.
- [60] F. Aligolizadeh, A. Hakkaki-Fard, A novel methodology for designing a multi-ejector refrigeration system, *Appl. Therm. Eng.* 151 (2019) 26–37.
- [61] O. Lamberts, P. Chatelain, N. Bourgeois, Y. Bartosiewicz, The compound-choking theory as an explanation of the entrainment limitation in supersonic ejectors, *Energy* 158 (2018) 524–536.
- [62] E. Schulz, M. Speekenbrink, A. Krause, A tutorial on Gaussian process regression: modelling, exploring, and exploiting functions, *J. Math. Psychol.* 85 (2018) 1–16.
- [63] H. Liu, J. Cai, Y.-S. Ong, Remarks on multi-output Gaussian process regression, *Knowledge-Based Syst* 144 (2018) 102–121.
- [64] A. Paramarzi, M. Heidarnejad, S. Mirjalili, A.H. Gandomi, Marine predators algorithm: a nature-inspired metaheuristic, *Expert Syst. Appl.* 152 (2020), 113377.
- [65] H. Rezk, A. Alahmer, R.M. Ghoniem, S. as' ad, boosting CO₂ uptake from waste concrete powder using artificial intelligence and the marine predators algorithm, *Processes* 11 (2023) 2655.
- [66] J.D. Filmlalter, L. Dagorn, P.D. Cowley, M. Taquet, First descriptions of the behavior of silky sharks, *Carcharhinus falciformis*, around drifting fish aggregating devices in the Indian Ocean, *Bull. Mar. Sci.* 87 (2011) 325–337.
- [67] M.S. Gritskevich, A.V. Garbaruk, F.R. Menter, A comprehensive study of improved delayed detached eddy simulation with wall functions, *Flow, Turbul. Combust.* 98 (2017) 461–479.
- [68] N. Ruangtrakoon, T. Thongtip, S. Aphornratana, T. Sriveerakul, CFD simulation on the effect of primary nozzle geometries for a steam ejector in refrigeration cycle, *Int. J. Therm. Sci.* 63 (2013) 133–145.
- [69] G.F.L. Al-Doori, Investigation of refrigeration system steam ejector performance through experiments and computational simulations, Ph.D. Dissertation, University of Southern Queensland, 2013.
- [70] S. Croquer, S. Poncet, Z. Aidoun, Turbulence modeling of a single-phase R134a supersonic ejector. Part I: numerical benchmark, *Int. J. Refrig.* 61 (2016) 140–152.
- [71] O. Lamberts, P. Chatelain, Y. Bartosiewicz, New methods for analyzing transport phenomena in supersonic ejectors, *Int. J. Heat Fluid Flow*. 64 (2017) 23–40.
- [72] X. Wang, J. Dong, G. Zhang, Q. Fu, H. Li, Y. Han, J. Tu, The primary pseudo-shock pattern of steam ejector and its influence on pumping efficiency based on CFD approach, *Energy* 167 (2019) 224–234.
- [73] A. Hemidi, F. Henry, S. Leclaire, J.-M. Seynhaeve, Y. Bartosiewicz, CFD analysis of a supersonic air ejector. Part I: experimental validation of single-phase and two-phase operation, *Appl. Therm. Eng.* 29 (2009) 1523–1531.
- [74] C. Wang, L. Wang, X. Wang, H. Zhao, Design and numerical investigation of an adaptive nozzle exit position ejector in multi-effect distillation desalination system, *Energy* 140 (2017) 673–681.
- [75] C. Li, Y. Li, W. Cai, Y. Hu, H. Chen, J. Yan, Analysis on performance characteristics of ejector with variable area-ratio for multi-evaporator refrigeration system based on experimental data, *Appl. Therm. Eng.* 68 (2014) 125–132.
- [76] B. Tashtoush, A. Alshare, S. Al-Rifai, Performance study of ejector cooling cycle at critical mode under superheated primary flow, *Energy Convers. Manag.* 94 (2015) 300–310.
- [77] D. Buttsworth, Calibration of a gas dynamic model for ejector performance. *ASTFE Digit. Libr.* Begel House Inc., 2017.
- [78] B. Gil, J. Kasperski, Performance estimation of ejector cycles using ethers and fluorinated ethers as refrigerants, *Appl. Therm. Eng.* 133 (2018) 269–275.
- [79] S. Kubacki, E. Dick, Simulation of plane impinging jets with $k-\omega$ based hybrid RANS/LES models, *Int. J. Heat Fluid Flow*. 31 (2010) 862–878.